Thunder Bay Regional Research Institute
Lakehead University

Dexter Hobson

Dual-modality Image Guided High Intensity Focused Ultrasound Device Design for Prostate Cancer: A Numerical Study

Dexter Hobson
2/2/2010

1

Abstract

In this study we established the feasibility of designing a multi-element high intensity focused ultrasound (HIFU) device for Magnetic Resonance and an ultrasound imaging-guided trans-rectal treatment of prostate cancer. An initial geometry was specified based on a clinical trans-rectal HIFU device with a central open space to lodge an independent ultrasound imaging probe for guidance. A parametric study was performed to determine the optimal focal length (L), operating frequency (f), element size (a) and central opening radius (r) of a device that would be capable of treating cancerous tissue within the prostate, spare the surrounding organs and minimize the number of elements. Images from the Visible Human Project were used to determine the organ sizes and treatment locations for simulation. Six virtual ellipsoidal tumors were located throughout a simulated prostate and their lateral and axial limit locations were selected as test locations. Using Tesla 1060(NVIDIA) graphics processors, the Bio-Heat Transfer Equation was implemented to simulate the heating produced during treatment at the test locations. L, f a and r were varied from 45 to 75mm, 2.25 to 3.00MHz, 1.5 to 8 times λ, where $\lambda = \dfrac{f}{speed\ of\ sound}$, and 9 to 12.5mm respectively. Results indicated that a combination of L, f, a and r of 68mm, 2.75MHz, 2.05λ and 9mm respectively could safely ablate tumors within the prostate and spare the surrounding organs. The number of therapeutic elements required for this device was 761.

Acknowledgements

I would like to thank Dr. Laura Curiel and Dr. Samuel Pichardo for the unique opportunity they gave me working as a graduate student and a research assistant at the Thunder Bay Regional Research Institute.

Contents

List of Figures

List of Tables

List of Symbols

Symbol	Meaning
c	Speed of sound in media for which it is propagating through (m/s)
f	Frequency (MHz)
λ	Wavelength (c/f)
ρ	Density (Kg/m^3)
T_α	Body Temperature (°C)
C	Specific Heat (J/Kg/°C)
χ	Acoustic Absorption Attenuation
ω	Perfusion Rate (Kg/m^3/s)
K_t	Thermal Conductivity (W/m/°C)
ι	Attenuation Coefficient (Np/m/MHz)

List of Abbreviations

Abbreviation	Meaning
BPH	Benign Prostatic Hyperplasia
DRE	Digital Rectal Exam
PSA	Prostate Specific Antigen
HIFU	High Intensity Focused Ultrasound
MRI	Magnet Resonance Imaging
CT	Computed Tomography
DNA	Deoxyribonucleic Acid
BHTE	Bio-Heat Transfer Equation
VHSMP	Visible Human Male Server Project
GUI	Graphics User Interface
CUDA	Computer Unified Device Architecture
PDT	Photodynamic Therapy
TOOKAD	Pd-Bacteriopheophorbide
LIIT	Induced Interstitial Thermotherapy
RITA	Radiofrequency Interstitial Tumor Ablation
CPU	Central Processing Unit
UI	Ultrasound Imaging
BCFSR	Bio-Chemical Free Survival Rate

Section 1: Background Information

Motivation

The Canadian Cancer Society predicts that prostate cancer will be the number one diagnosed cancer in Canadian men (25,500 new cases predicted for 2009) and will have the third highest cancer mortality rating in the year 2009 (4,400 deaths predicted for 2009) of all cancer types in men (Public Health Agency of Canada).The Canadian Cancer society predicts that 9,900 men at an age from 60-69 years old will be diagnosed with prostate cancer in the year 2009 (Public Health Agency of Canada). This represents the highest number of cases of all age groups for men. The second highest number of predicted cases in the year 2009 is for the age group of 70-79 years old totaling 6,700 men (Public Health Agency of Canada). The third highest number of predicted cases in the year 2009 is for the age group of 50-59 years old totaling 5,000 men (Public Health Agency of Canada).

There are many current treatment options for prostate cancer patients. A relatively new treatment option for patients diagnosed with early stage prostate cancer is trans-rectal High Intensity Focused Ultrasound (HIFU) (Crouzet S., 2010). Two trans-rectal HIFU systems are currently available; the Ablatherm^{TM} (EDAP-TMS, Vaux-en-Velin, France) and the Sonablate®-500 (SB-500; Focus Surgery, Inc., IN, USA). These two systems are intended to ablate the entire prostate without affecting surrounding organs. The most common associated morbidity for treatment with both the Ablatherm^{TM} and the Sonablate®-500 systems is partial or total loss of potency (%43.2 of patients). Other reported effects are stress incontinence (%5.7), urinary tract infections (%7.1), chronic or pelvic pain (%5.7) and in more rare cases rectourethral fistula (%2.2) (Uchida T., 2006, Poissonnier L., 2007, Rouviere O, 2007, Blana A., 2008, Netsch C., 2010). Most of these effects are a result of treating the entire prostate. They can be significantly reduced by treating only specific areas of the prostate and therefore reducing the amount of ablated tissue. This will not only result in less morbidity but it will shorten the recovery times. This can be achieved by using a device capable of dynamically focusing the energy to limit the treatment to the tumor masses within the prostate and not damage surrounding prostatic tissue and other structures.

Current clinical trans-rectal HIFU treatment systems use ultrasound imaging for treatment planning and targeting (Illing R., 2006, Poissonnier L., 2007). An ultrasound imaging transducer is used to determine the location of the prostate and plan the treatment locations. The imaging transducer is either permanently fixed in the center of the treatment applicator or it is inserted for treatment planning and then retracted during treatment. Another type of imaging that has proven quite useful for real time feedback during HIFU treatment is Magnetic Resonance Imaging (MRI) (Chapman A., 2007). MRI allows for targeting while providing with thermal information during treatment. Thermometry can be achieved by the phase shift of the protons signal caused by the temperature changes that can be retrieved using the MRI.

The device proposed in this study is designed to be compatible with both MRI and ultrasound imaging guidance. Using both of these modalities will give physicians more control over the HIFU treatment and result in more accurate ablation of tumors. Besides, having both imaging modalities will allow for the validation of other novel imaging techniques for the estimation of HIFU effects based on those modalities (Curiel L., 2009).

In this first section an overview of the specifications for the designed device will be presented. The anatomy of the prostate and surrounding tissues will be explained followed by the explanation of prostate cancer and its diagnoses. Current treatment options will be then detailed with their benefits and disadvantages. Then the underlying concepts of HIFU will be introduced as well as the currently available HIFU treatment options for prostate cancer.

The Prostate Gland

The prostate is part of the urinary tract and the reproductive system as seen in Figure 1-1 (Martini H., 2005). The prostate is located inferior of the bladder in the urinary tract. The urethra passes urine by the contraction of the urogenital diaphragm which is located inferior and posterior to the prostate gland. The urogenital diaphragm consists of two circular bands of skeletal muscles which are called the external and internal urethral sphincters. The external urinary sphincter is located inferior to the prostate gland. It is the only voluntary controlled sphincter of the urogenital diaphragm and it must be relaxed to allow urination. The internal urinary sphincter is located superior of the prostate gland and is not under voluntary control. The urethra connects the urinary bladder to the penis and hence extends from the neck of the urinary bladder to the tip of the penis. When the urethra passes through the prostate it is named the prostatic urethra. The prostatic urethra is completely encapsulated by prostatic tissue.
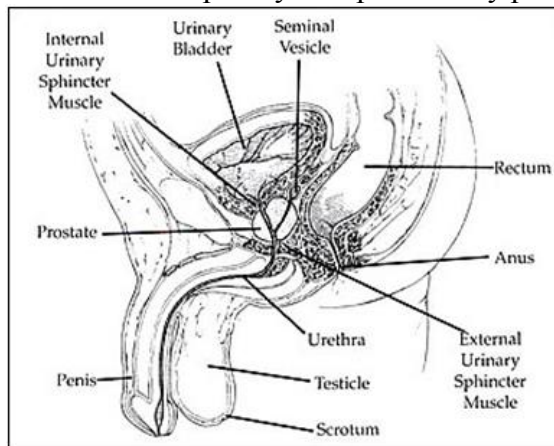
Figure 1-1. Prostate Gland Anatomy

The prostate gland is also part of the reproductive system as one of the accessory glands. The functions of the accessory glands are to activate spermatozoa, provide the nutrients the spermatozoa need for motility and produce buffers that counteract the acidity of the urethral and vaginal contents. These glands include the seminal vesicles, the prostate gland and the bulbourethral glands. The prostate gland is the largest of the accessory glands. It is a muscular organ with a normal volume of 20 ml although it can grow up to five or six times this volume with increasing age. The prostate gland consists of connective tissue, muscle and prostatic glands. The prostatic glands produce a weakly acidic secretion which includes several compounds including seminalplasmin which is an antibiotic which may help prevent urinary tract infections in men (Martini H., 2005). This secretion is caused by peristaltic contractions of the muscular structure of the prostate gland. The prostate gland also encircles the ejaculatory duct. The ejaculatory ducts connect the ductus deferens and the seminal vesicles to the urethra. The ductus deferens pass posterior curving inferiorly along the lateral surface of the urinary

bladder toward the superior and posterior margin of the prostate gland. The ductus deferens transport spermatozoa to the ejaculatory ducts from the epididymis by peristalsis, as well as store spermatozoa. The seminal vesicles contribute 60% of the volume of semen specifically containing prostaglandins, clotting proteins and fructose. This composition gives spermatozoa nutrients and energy to mature into sperm, and is also passed by peristalsis. The bulbourethral glands are located inferior to the prostate gland, posterior to the urethra, superior to the base of the penis and are covered by the fascia of the external urethral sphincter. The bulbourethral glands are round in shape with a diameter approaching 10mm. The ducts of the bulbourethral glands are parallel to the urethra as it travels through the penis. The bulbourethral glands secrete thick alkaline mucus which helps to neutralize urinary acids in the urethra of the man and the woman and provides lubrication for the tip of the penis during intercourse (Martini H., 2005).

The prostate has an anterior, posterior and two inferolateral surfaces. The superior portion of the prostate is known as the base, and the inferior portion is known as the apex. There is a midline depression on the posterior and superior surface of the prostate. Fat tissue is found anterior to the prostate in the retropubic space. Inferior of the prostate is the external urinary sphincter. The Denonviller' fascia, which is posterior to the prostate, separates it from the rectum. The inferolateral surfaces of the prostate rest on the pubis bone. The prostate is partially enveloped by the prostatic capsule. The prostatic capsule is the outer non-glandular portion of the prostate. The prostatic capsule is attached to the posterior border of the pubic bone by the puboprostatic ligaments. These ligaments are attached to the prostatic capsule on either side of the apex of the prostate and the pubis. Superior of the prostate is the internal urinary sphincter, the urinary bladder, the urethra, the ejaculatory ducts and the seminal vesicles.

Urine travels through the prostatic urethra and seminal fluid travels through the ejaculatory ducts and the urethra. The ejaculatory ducts pierce the posterior and superior portion of the prostate. After travelling approximately 2cm through the prostate the ejaculatory ducts meet with the prostatic urethra at the verumontanum.

There are three main zones usually referred to in the prostate. The three zones are the peripheral, central and the transition zones (see Figure 1-2).
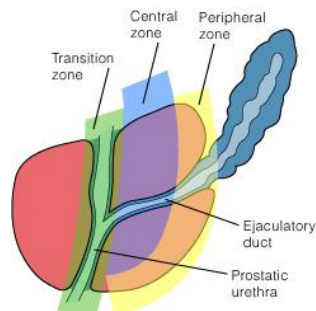
Figure 1-2. Sagital view of prostatic zones

The peripheral zone is the posterior and lateral zone of the prostate and represents about 70% of the glandular portion of the prostate. The central zone represents 25% of the prostate gland. The ejaculatory ducts are located in the middle of the central zone. As seen in Figure 1-11 the inferior portion of both the central and peripheral zones do not include the entire prostate. The reason for this incomplete inclusion is that the inferior and anterior portion of these zones is embedded into the fibromuscular stroma. The transition zone represents between 5% and 10% of the prostate. It surrounds the urethra and is comprised of two independent smaller lobes. The remainder of the

prostate is noted on Figure 1-11 in red and is the anterior section of the prostate. This section is named the ventral fibromuscular zone and is not considered a glandular structure. It is the largest single component of the prostate, representing one third of the prostate volume, and includes the apex of the prostate.

Figure 1-3 shows a transverse view of the prostate gland. The nerves supply for the prostate comes from the spine. The nerves travel outside the prostatic capsule and Denonvilliers' fascia until they perforate the capsule at the point of entry. The neurovascular bundle supplies part of the nervous system for the prostate and the penis. It is separated from the prostate by 1.5mm at the base and 3mm at the apex. These nerves are part of the erectile function and if severed or damaged could result in erectile dysfunction (Kirby S., 2000). The prostate is also divided into five lobes. These five lobes are the two lateral lobes, the anterior lobe, the median lobe and the posterior lobe (Figure 1-3). These lobes are held together by the prostatic capsule. The lateral lobes partially encircle the urethra, the ejaculatory glands and the anterior lobe. The anterior lobe is located anterior of the urethra. The median lobe is located posterior to the urethra and anterior to the posterior lobe. The posterior lobe is the most posterior lobe of the prostate and is closest to the rectal wall. The rectum and rectal wall is located posterior of the prostate.
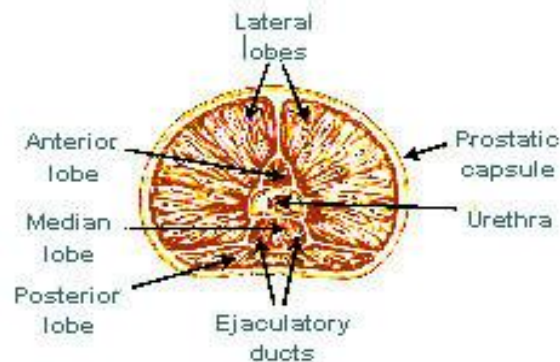
Figure 1-3. Five lobes of the prostate

Common Prostate Pathologies

Benign Prostatic Hyperplasia

A common prostate pathology is Benign Prostatic Hyperplasia (BPH). BPH is the enlargement of the prostate. This benign growth does not spread to other parts of the body, but BPH can enlarge the prostate enough to obstruct the urethral outlet (Black M., 2009) causing urine retention. Treatments for this type of abnormal growth include inserting a catheter to allow urine flow from the bladder, hormonal modulation to lessen the growth of the prostate and if necessary partial removal of some of the prostatic tissue.

Prostate Cancer

Prostate Cancer Cells

Prostate cancer is the malignant growth of cancer cells in the prostate. Prostate cancer cells are highly proliferative, less differentiated than normal cells, and exhibit altered cellular adhesion (Tu H., 1996, Kirby S., 2000). Due to their altered cellular adhesion they are able to metastasize to other parts of the body throughout the lymphatic system or blood stream and initiate formation of secondary tumors (Kirby S., 2000). There are two main manners in which cells die. These two manners are necrosis and apoptosis. Necrosis is usually a premature cell death caused by some external factor such as infection or trauma. Apoptosis is the natural death of cells. Cancer is caused by a deregulation on this natural cycle of the cell life. Cancer cells do not undergo apoptosis and can accumulate in the tissue that they are inside and create a tumor. In early stages of prostate cancer it is the inability to perform apoptosis which is more critical to the growth of the tumor (Tu H., 1996).

Diagnoses

Physicians have three main methods to diagnose prostate cancer. They are the digital rectal exam (DRE), the prostate specific antigen (PSA) test and imaging. The DRE is part a physical exam for males and may also be used on female patients. The DRE is performed to check for problems with organs in the pelvis and lower abdomen. A physician applies a lubricant to a gloved hand and gently inserts it into the rectum of the patient. The physician may use the other hand to move organs around to check them as well. In regards to the prostate gland the physician is looking for enlarged size of the prostate or hard lumps of tissue within the prostate. Hard lumps in the tissue could indicate prostate cancer since prostate tumors are usually harder than regular prostatic tissue. Another indicator of irregular cell activity in the prostate is the amount PSA in the blood stream. PSA is a protein produced by the prostate and is found in small quantities in the blood. A blood sample is taken from the patient and the quantity of PSA in the blood is measured.

There are a number of issues in choosing a normal PSA level. The problems associated to this choice are a standardized measuring system and that every patient may have different normal levels. De Angelis *et al.* (2007) writes that if a PSA measurement higher than 2.5ng/ml is recorded than a biopsy should be considered for the patient according to the National Comprehensive Cancer Network of the United States (DeAngelis G., 2007). A more realistic approach to this problem is to measure the PSA frequently and consider a biopsy if the levels change dramatically from one test to the next. A prostate biopsy occurs when a physician and a patient are suspect to cancerous growth within the prostate. A prostate biopsy is a procedure in which samples of the prostate are removed for examination by a pathologist to look for evidence of cancer cells in the prostate. It is also known as the prostate needle biopsy because an 18-gauge needle is inserted either through the urethra, the rectum or the perineum to remove test tissue from the prostate. The prostate needle biopsy is the most effective diagnoses for prostate cancer (Kirby S., 2000). A prostate biopsy can be performed under the guidance of ultrasound or magnetic resonance imaging (D'Amico A.V., 2000). Ultrasound guidance of prostate biopsy is performed by inserting an ultrasound imaging device into the urethra, the abdomen, the perineum or the rectum. The most widely used technique for imaging guidance of a needle biopsy in the prostate is to trans-rectal imaging, since it provides the most useful diagnostic information, and it is the most precise method for guiding the needle to its preferred site (Melchior S.W., 1996).

There are four levels of prostate cancer named T1, T2, T3, and T4. T1 represents a tumor that is too small to see on a scan or physical exam, but may be seen in a needle biopsy or be seen through higher prostate specific antigen (PSA) levels, both the needle biopsy and PSA will be explained further in this report. T2 has three levels of diagnoses. First being when the tumor is only in half of one of the lobes of the prostate, second level being when the tumor is in more than half of one of the lobes, and the final level of T2 prostate cancer is when the tumor is in two or more lobes of the prostate but still contained in the prostatic capsule. T3 is the level at which the cancer has broken through the prostatic capsule. T4 is the level at which the cancer has affected other organs or tissue other than the prostate. This is the level in prostate cancer in which metastasis occurs. At this level the cancer cells are able to travel within the lymphatic system or the blood stream and are able to create secondary tumors at other sites within the body.

Pathologist's use the Gleason grading system to evaluate the progression of a tumor sample collected in a biopsy (Kirby S., 2000). The Gleason grading system is based on the architectural patterns of the primary and secondary cancerous tissues (first and second most occurring patterns) in the sample taken in the biopsy (Kirby S., 2000). The patterns are given a grade from one to five, one representing glands that are the most differentiated and five representing glands that are the least differentiated. Figure 1-4 is a picture of the gland architecture represented by the Gleason score. The total Gleason score is the addition of both the Gleason score of the primary and secondary architectural patterns. If there is only one architectural pattern in the sample it will determine the primary and secondary Gleason score. Total Gleason scores range from two to ten. A score of one is given in the Gleason grading system for a pattern with glands that are of medium size, single, separated, closely packed and are uniformly shaped. A Gleason grade of two represents glands that are still single and separate, but are not as uniformly shaped as those of a Gleason score of one. A Gleason score of three represents a sample that has infiltration into the non-neoplastic tissue from the neoplastic tissue. The glands are of irregular shape and size as compared to those in a Gleason score of one or two, but are still single. A sample with a Gleason score of four has glands that are no longer single and are beginning to form large irregular glands as compared to those glands in a Gleason score of one to three. A Gleason score of five represents a sample that has almost no glandular differentiation. The tumors in these samples are composed of solid cords, or single cells.
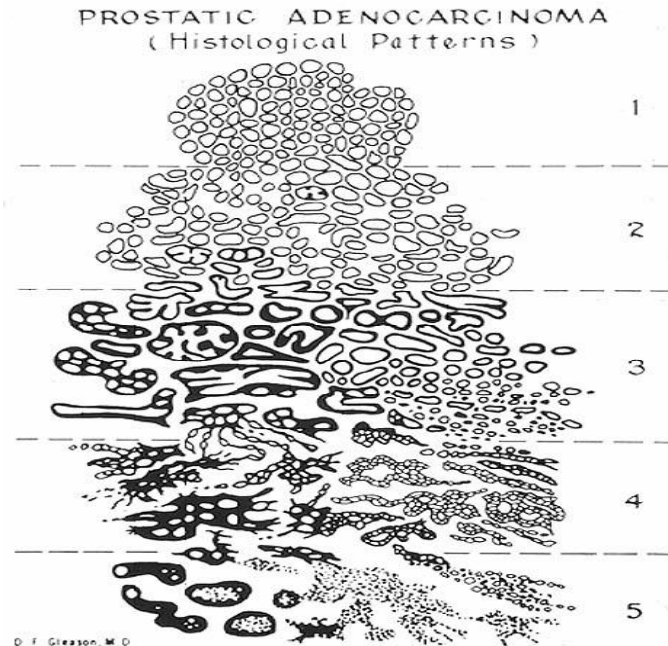
Figure 1-4. Representation of cell architecture in Gleason scoring system

Current Treatment Options

There are many treatment options for patient diagnosed with prostate cancer. Watchful waiting is the first option for patients with T1 prostate combined with hormonal therapy. (Chodak Gerald W., 1994) The five most commonly used treatments for prostate cancer are brachytherapy, external beam radiation therapy, prostatectomy, chemotherapy or high intensity focused ultrasound (HIFU). In all of these treatment options the prostate must be imaged to determine its location and current clinical state. This imaging is performed using ultrasound, MRI or Computed Tomography (CT) imaging.

Prostatectomy

Prostatectomy is the full or partial removal of the prostate gland. The procedure is used for local prostate cancers only. If the cancer has metastasized, T4 level of prostate cancer, then this treatment is not worth performing as it will only solve a local problem. Radical prostatectomy is the most recommended surgery for prostate cancer (Prostate Cancer Canada Network, *Surgery*, 2009). There are three types of radical prostatectomy in practice today named radical retropubic prostatectomy, radical perineal prostatectomy and robotic radical prostatectomy. Radical retropubic prostatectomy is performed by making an incision from below the navel to above the pubic bone in the middle of the patient. The surgeon than removes the prostate, the seminal vesicles and the prostatic urethra. After these tissues have been removed the surgeon connects the remaining part of the urethra to the bladder and inserts a catheter to help the urethra heal properly. Radical perineal prostatectomy is performed the exact same way as radical retropubic prostatectomy except that the incision is made between the scrotum and the anus. This surgery is commonly used for patients who have had previous abdominal surgeries and have extensive scar tissue on their abdomen. Radical retropubic protatectomy is the preferred surgery as it provides a better view of the bladder (Prostate Cancer Canada Network, *Surgery*,

2009). Erectile dysfunction is a common side effect of a radical prostatectomy procedure. A working erection is possible within four to twelve months after surgery and often may take up to two years before the nerves recover from the surgery (Prostate Cancer Canada Network, *Surgery*, 2009). Erectile function may not be possible if the nerves are extensively damaged which occurs in %57.5 to %71.2 of patients whom chose this treatment option (Siegel T., 2001).

For these surgeries the surgeon can choose to implement nerve sparing techniques, to allow erectile function as discussed earlier, by cutting very close to the capsule of the prostate and perhaps leave some of the prostatic tissue in the patient. This procedure is not possible for all patients because if the tumor is too close to the nerves it will be extremely difficult to remove it without damaging these nerves and if some of the prostate is left it could also leave some of the cancer cells. The most evident side effect of this procedure is infertility. The patient can still have an orgasm but his ejaculation will be dry since the vas deferens, ejaculatory ducts and prostate are no longer connected to the urethra. Urinary incontinence is a common side effect after a radical prostatectomy but after 24 months %95 of patients regain urinary control (Eastham J.A., 1996).

External Beam Radiation Therapy

External beam radiation therapy treatment begins with treatment planning. Using CT or MRI images the location and size of the prostate is determined. These images are then used to define the treatment area and once this area is defined treatment planning is conducted to determine the radiation dosages and locations of the dosages. A linear accelerator is used to administer these doses. An image of a linear accelerator is seen in Figure 1-5. These devices are in a lead and concrete walled room to ensure that their radioactive doses do not leave the room.

Figure 1-5. Image of a Linear Accelerator

A medical linear accelerator treatment platform consists of a bed for the patient and the linear accelerator itself. There are a number of linear accelerators available for medical use. The most commonly used accelerators for prostate cancer produce high energy x-rays. These x-rays are produced by accelerating electrons in a waveguide and then colliding these electrons with a heavy metal. This collision produces the x-ray energy. The x-rays are directed at the patient and

19

are formed using either specifically shaped lead blocks, or a multi-leaf lead collimator. Both of these directional options are incorporated into the head of the machine. The beam of x-ray energy comes out of the gantry (see Figure 1-5). The gantry is able to move completely around the patient allowing any angle for the beam. The bed is also able to move in any direction to assist in proper placement of the patient. Lasers are used to help align the patient whom is given permanent tattoos or marked with stickers to ensure that they are properly placed on the bed. This treatment is usually administered Monday to Friday for five to nine weeks depending on the severity of the cancer (Kirby S., 2000). Having the weekend free of treatment allows the non-cancerous cells time to recover from the treatment as they are also being exposed to the radiation. Side effects of this treatment include severely urgent bowel movements (%9 after 24 months), loss of urinary control (%3 after 24 months) and erectile dysfunction (complete dysfunction in %39.6 of patients after 24 months) (Hamilton A.S., 2001).

Brachytherapy

Brachytherapy and external beam radiation therapy both use doses of radiation to cause double stranded DNA breaks in cancer cells. These double stranded breaks occur both in the cancer cells and in non-cancerous cells. The reasons that most non-cancerous cells are not killed during this process of radiotherapy are that non-cancerous cells repair, reoxygenate, reassort, and repopulate better than cancer cells after radioactive treatment (Kirby S., 2000). To treat tumors using brachytherapy an extensive treatment plan needs to be completed with information taken from ultrasound, CT or MRI images. This plan will govern the amount of radiation to be administered to certain areas of the prostate and how it will be administered. The two brachytherapy treatment types for prostate cancer are permanent seed implant brachytherapy and temporary brachytherapy. Permanent seed implant brachytherapy involves implanting seeds of radioactive material, commonly used isotopes are Iodine-125 and Palladium-103, into the prostate. Once implanted the seeds decay and emit gamma rays. These gamma rays are responsible for creating the double stranded breaks in the DNA of the cancer cells and non-cancerous cells. Figure 1-6 shows an X-ray image of a patient who has permanently implanted seeds in his prostate. The other treatment using brachytherapy is temporary brachytherapy. Temporary brachytherapy is performed by inserting catheters into the prostate gland as seen in Figure 1-7. Once inserted inside the prostate gland the catheters can be used in a series of radiation treatments to provide certain doses to certain areas on the prostate.
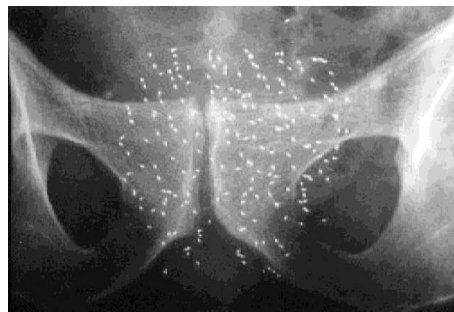
Figure 1-6. X-Ray of permanent seed implant brachytherapy

Radioactive seeds are placed inside the catheter for a pre-determined amount of time and then removed. After the procedure the catheters can be removed and there is no permanent radioactive material left inside the prostate of the patient.

Figure 1-7. Catheter insertion for temporary brachytherapy

The side effects to this treatment are similar to those of the external beam radiation therapy treatment because, just as in external beam radiation therapy, the healthy tissues are being exposed to radiation as well. The difference between brachytherapy and external beam radiation therapy is that the radiation is more concentrated within the prostate thus decreasing the radiation dosage to surrounding tissues. Side effects from brachytherapy include impotency (%13 of patients after 6 months), urination changes including increased frequency (%40 of patients after 6 months) and burning during urination (%17 of patients after six months) (Arterbery V.E., 1997).

Chemotherapy

Chemotherapy refers to treatment performed using chemically based drugs. In the treatment of prostate cancer, chemotherapy is used when metastasis has occurred (T4 prostate cancer). Chemotherapy drugs are toxic and systemic (Prostate Cancer Canada Network, *Chemotherapy*, 2009). They affect cells that are constantly and quickly proliferating. These cells include cancer cells, hair cells and finger nail cells. These drugs may be used in conjunction with the other treatments but are only used to slow cancer growth and not expected to stop it (Prostate Cancer Canada Network, *Chemotherapy*, 2009). The most common uses of these drugs are to elongate and better life for as long as possible. Side effects for chemotherapy treatment include hair loss, finger nail loss, nausea, vomiting diarrhea and mouth sores. Chemotherapy can also damage white blood producing cells in bone marrow (Prostate Cancer Canada Network, *Chemotherapy*, 2009) and therefore have an effect on the patient's ability to fight infection and show side effects such as anemia and fatigue.

New Treatment Options

There are a number of future treatment options in investigation for the treatment of prostate cancer including cryotherapy, photodynamic therapy, laser induce interstitial

thermotherapy and radiofrequency interstitial tumor ablation. In this section these future options will be discussed individually.

Cryotherapy

Cryotherapy is a treatment in which the cancerous tissue is cooled to $-40^{\circ}C$ to induce cell death by freezing to the entire prostate. There are three generations of cryosurgery that have been implemented beginning in the 1960's with liquid nitrogen being used to freeze tissue without guidance or urethral warmers. The complications of this surgery were significant and included incontinence and rectourethral fistula (Han, K.R., 2003). The second generation of cryotherapy began in the late 1980's and early 1990's and included transrectal ultrasound guidance and urethral warmers which lessened the morbidities associated with this procedure. The recent generation of cryotherapy uses smaller probes, 1.5mm in diameter, to deliver argon gas and helium gas to reheat the tissue (Chin, J.L., 1998). The probes are inserted into the perineum using a technique similar to brachetherapy. Thermocouples are also inserted through the perineum to tract the cooling of the prostate and to ensure surrounding tissue structures, such as the neurovascular bundle, are not affected. A catheter is also inserted into the urethra to ensure that none of the needles pierced the urethra during insertion and to warm the urethra during the procedure. Once all of the surgical equipment is in place the patient undergoes a freeze and thaw cycles to destroy the tissue. This cycle can be repeated in a particular region if the physician deems it appropriate and for larger prostates the probes and thermocouples are moved to treat the larger area.

Han *et al*. (2003) treated 106 patients and had a 12 month period of PSA follow-up. All patients were discharged within 24 hours after of the procedure. Associated morbidities of this treatment included urinary retention (%3.3), impotency (%87 of previously potent patients), and incontinence (%8). After 12 months %75 of patients had a PSA of 0.4ng/ml. Another multicenter study is ongoing to determine long term effects and success of this type of treatment.

Photodynamic Therapy

Photodynamic therapy (PDT) is conducted by first injecting a drug which can be locally controlled by a light source. When activated by the light source these drugs create reactive oxygen species which results in tissue necrosis. An application which is being investigated is using photodynamic therapy for the treatment of localized prostate cancer. Koudinova *et al*. (2003) used Pd-Bacteriopheophorbide (TOOKAD) dissolved in Cremophor EL-based vehicle as the drug to create the reactive oxygen species in the mouse model for photodynamic therapy with TOOKAD (Koudinova, N.V., 2003). The mice in this study were implanted with a prostate cancer tumor. The tumors were then grown in the mice until they had reached a desirable size. Then the mice were injected with TOOKAD and the tumor was exposed to one of two light sources which had a wavelength of 650-800nm and 770nm, respectively, for 30 minutes. In total %69 on the mice in this study did not re-grow the tumors after 90 days.

Huang *et al*. (2005) conducted a similar study in the canine model in which 19 healthy canines and 1 with prostate cancer were used to test TOOKAD-PDT. The dogs in this study underwent a laparotomy procedure (Chen, Q., 2002). One week post surgery the healthy canine

prostates were removed and it was determined that the peripheral zone of the prostate was destroyed with tissue damage extending into the prostatic capsule and surrounding muscular tissue. The cancerous canine prostate had a %25 reduction in volume but the bog died 1 week after due to the spread of the disease.

Laser Induced Interstitial Thermotherapy

In Laser Induced Interstitial Thermotherapy (LIIT) a laser probe is used to deliver laser light to tumor locations within the prostate and the absorption of this light causes the tissues at the target site to be ablated. Two patients with localized prostate cancer have been successfully treated with a 1.6mm laser probe (Raz, O., 2010). The tumor locations for both patients were determined using MRI imaging and biopsies. Under MRI guidance, an MRI compatible metal catheter was inserted into the perineum of each patient using an insertion technique similar to brachetherapy. Once the catheter was in the correct position it was replaced by the laser applicator. The laser applicator was activated and using MRI thermometry, which will be discussed later in this report, the physician was able to track the heating of the prostatic tissue. The patients were imaged post-surgery and it was decided to repeat the procedure due to residual vascularization and shortly after the patients were discharged. MRI scans were conducted two weeks after the procedure and no evidence of complications were found. Also one month after the procedure no adverse effects were reported by the patients. Follow-up biopsies are planned for 6 months after the treatment to determine the efficacy of the treatment.

Radiofrequency Interstitial Tumor Ablation

Radiofrequency Interstitial Tumor Ablation (RITA) technology uses radio frequency applicators to create heat within the tissue and create irreversible tissue damage through coagulative necrosis. Shariat *et al.* (2005) conducted a pilot study to determine the efficacy of this treatment for prostate cancer. The radio frequency applicators used in this study were 15-gauge quadralupe-hook needle probes. The operating frequency of these applicators was 460KHz. Eleven patients with non metastatic prostate cancer were included in this study. Before the procedure, physicians determined the cancerous tissue within the prostate through biopsies. For the RITA procedure a catheter was inserted into the urethra and cooled with liquid. Thermocouples were inserted into the prostatic tissue and surrounding tissue to measure temperature change. A transrectal ultrasound imaging probe was inserted for guidance and the radio frequency applicators were inserted into the prostate through the perineum using a technique similar to that of brachytherapy. The power of each applicator was raised in a stepwise manner until the temperature of the tip of the applicator reached $100^{O}C$ and then was kept at this temperature for five minutes. 33 lesions were created in the 11 patients with four patients having two lesions, two having three lesions and four having four lesions. Twelve months after RITA %67 of the patients were negative for prostate cancer in the RITA treated locations following

biopsy. No severe complications were reported in this study but one patient experience bladder spasms for a week post RITA, another experienced burning during urination for a week post RITA and one patient had an episode of moderate constipation.

High Intensity Focused Ultrasound

Overview

High Intensity Focused Ultrasound refers to a treatment in which ultrasound waves are focused within the body causing a temperature elevation and thermal ablation of tissues. Ultrasound waves are mechanical waves with a frequency higher or equal to twenty kilohertz and are produced by a transducer. Transducers produce these sound waves through mechanical vibration (Hill C.R, 2004). These vibrations cause movement of the particles in the media in which the sound waves are propagating through. This particle movement creates the pressure waves which represent the acoustic energy of the source (transducer). The acoustic energy is focused by using a constructive interference pattern of acoustic waves. This interference pattern is created with natural geometrical focusing or with electrically dynamic focusing. This results in acoustic pressures much lower at locations in the near and far field and higher pressures at the focal region as seen in Figure 1-8.
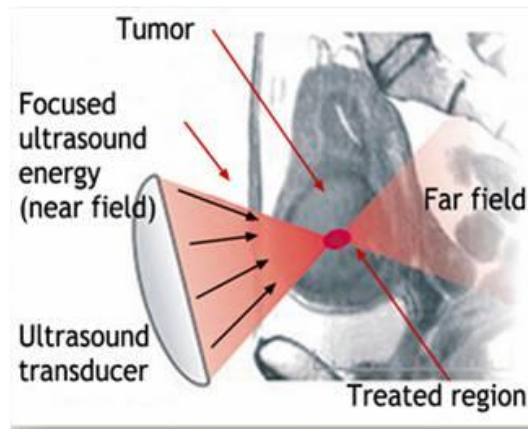
Figure 1-8. HIFU near and far fields

The tissue at the focal region experiences a high increase of temperature which creates irreversible tissue necrosis (Lele, 1967). Through this phenomenon tissues at the focal region can be ablated with minimal affects to surrounding tissues.

There are two ways to adjust the focal point of a transducer in body cavities: mechanical and electronic. The mechanical focusing implies the physical construction of a device shaped to make convergence of the ultrasound waves at a desired location. The second is electrical dynamic focusing (Diederich C.J., 1991, Chapelon J.Y., 1993). Electrical dynamic focusing uses an array of transducers to enable control of the phase of the signal to each transducer to cause the maximum summation of wave acoustic energy at the desired location (Von Ramm O.T., 1983). This is known as steering the acoustic field. In literature, and in the following study, each transducer in the array is referred to as an "element" while the whole array is referred to as the "transducer". Figure 1-9 demonstrates how electrical dynamic focusing can create a focal point from a flat array transducer.
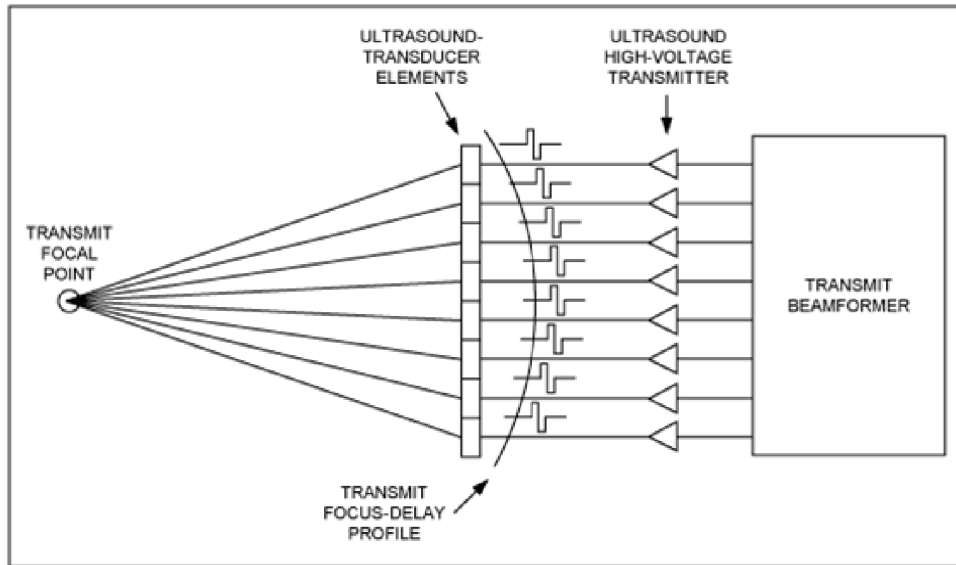
Figure 1-9. Electrical Dynamic Focusing

There are several methods to calculate the phase of each element in order to dynamically steer the focal point (Curiel L., 2001). In this study the phase required for each element is determined by back propagating a spherical wave from the desired treatment location to each element (Pichardo S., 2009).

The placement of the elements in a transducer array is crucial. If the elements are not spaced properly grating lobes can occur. Grating lobes are caused by undesirable acoustic wave summation at points within the tissue other than the treatment area. If the deposited acoustic energy is too high at the locations other than the treatment location undesired heating can occur and if high enough this type of heating causes what is commonly referred to as secondary lesions. A concentric array with consistently sized array elements can produce grating lobes if the elements are not spaced properly. Figure 1-10 is an image of a linear planar array of transducer elements. The angle between the first grating lobe and the primary lobe is θ. This angle can be calculated using equation 1-1. In equation 1-1 m is the number of the grating lobe for which θ is being calculated for, in Figure 1-10 $m = 1$, Δx is the distance between the centers of two neighboring elements, and λ is the sound propagation speed for the media, divided by the operating frequency of the device.
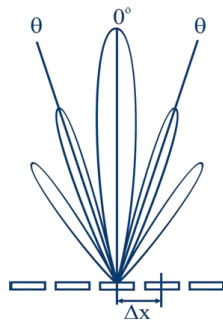
$$\sin\theta = \frac{\lambda}{\Delta x} \qquad\qquad (1\text{-}1)$$

Figure 1-10. Planar Array with Grating Lobes

It can be seen in equation 1-1 (Curiel L., 2001) that if $\Delta x = \lambda$ then $\theta = 90^0$ and the grating lobe is eliminated. By reducing the space between elements to less than λ (choosing a Δx less than λ) the

first grating lobe can be eliminated and the possibility of secondary lesions being produced by grating lobes can be eradicated.

Biological Effects

Ultrasound waves are known to have two major effects on biological tissue when propagating through them, which are mechanical absorption and cavitation (Curiel L., 2001, Chavrier F., 2000). Absorption is a component of attenuation and is the conversion of ultrasound energy into heat within the media the ultrasound energy is propagating through (Hill C.R, 2004). The percentage of sound that is effectively absorbed into tissue is expressed by the acoustic absorption coefficient, χ, and is found experimentally in many different tissues for use in calculation. The attenuation of ultrasound is exponentially related to the product of frequency of the wave and the depth into the tissues. The deeper into the tissues the more the energy will be attenuated, and for higher frequencies this attenuation will also be more important (Bamber J.C., 1979).

The heat distribution within tissue can be calculated using Pennes' Bio Heat Transfer Equation (BHTE) (Pennes H.H., 1948), given by

$$\rho_t C_t \frac{\partial T_P(x,y,z,t)}{\partial t} = K_t \nabla^2 T_p + \omega_s C_s (T_s - T_p) + Q_p \qquad (1\text{-}2)$$

where: ρ_t = tissue density $\left(\frac{kg}{m^3}\right)$

C_t = specific heat capacity of tissue $\left(\frac{\frac{J}{kg}}{\,^\circ C}\right)$

T_p = temperature at point $P(x,y,z)$ at time t

K_t = thermal conductivity of tissue $\left(\frac{\frac{W}{m}}{\,^\circ C}\right)$

ω_s = perfusion rate of blood $\left(\frac{\frac{kg}{m^3}}{s}\right)$

C_s = specific heat of blood $\left(\frac{\frac{J}{kg}}{\,^\circ C}\right)$

T_s = temperature of blood

Q_p = energy intake at point $P(x,y,z)$ from external source $\left(\frac{W}{m^3}\right)$

with: $\nabla^2 T_P(x,y,z,t) = \frac{\partial^2 T_P}{\partial x^2} + \frac{\partial^2 T_P}{\partial y^2} + \frac{\partial^2 T_P}{\partial z^2}$

$Q_p = \chi \frac{E_o - E}{V}$

where: E_o, E = acoustic energy entering and exiting the volume V respectively

χ = acoustic absoprtion coefficent

$E = \frac{1}{2}\rho c v_o^2$, v_o = maximum particle velocity

The BHTE is a modification to the basic thermodynamic equation of energy conservation and is composed of three major components which are the heat conduction of the tissue

$K_t \nabla^2 T_p(x, y, z, t)$, heat transfer from blood perfusion of the tissue
$\omega_s C_s [T_s(x, y, z, t) - T_p(x, y, z, t)]$ and the absorbed acoustic energy $Q_p(x, y, z, t)$. The temperature increase produced by this external heat source can create irreversible tissue damage. The temperature required to produce irreversible tissue damage is a function of the exposure time (Lele P.P., 1967).

Figure 1-11 shows the relationship between temperature and time for which irreversible tissue damage can occur. For low temperatures or short exposure times the tissue is capable of dissipating the heat by perfusion or conduction away from the application site and therefore the tissue remains undamaged and can return to its natural temperature and state. Tissue that is exposed to higher temperatures or relatively long exposure times can be irreversibly damaged due to heat accumulation. The grey area in Figure 1-11 represents tissue that can be damaged differently based on the nature of the cells that are being exposed.
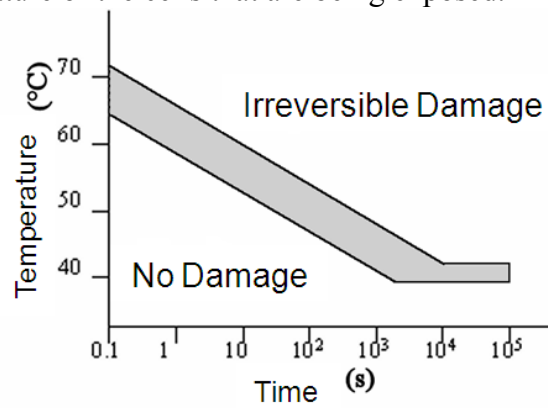
Figure 1-11. Tissue Damage as a Function of Time and Temperature

When the transducer is excited, the temperature of the tissue being treated begins to increase at an exponential rate and once the transducer is de-energized the tissue begins to cool at an exponential rate. Figure 1-12 is the simulated temperature versus time at the focal point of a simulated HIFU transducer. At time t=5s the simulated transducer was de-energized and the temperature at the focal point begins to drop.
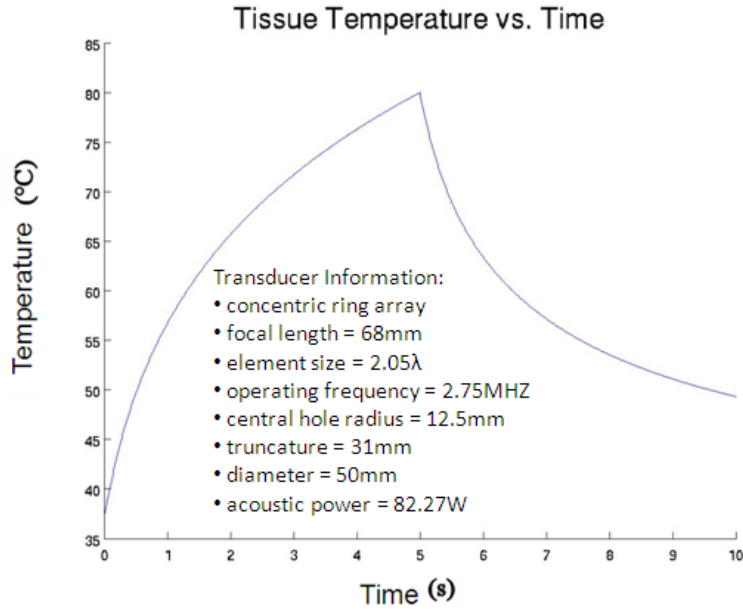
Figure 1-12. Tissue temperature versus time during HIFU exposure of 5s (In this simulation the transducer was centered in a coolant ellipse filled with water with major and minor diameters of 3.9cm and 2.6cm, respectively which was inside of a distended rectum ellipse with major and minor diameters of 4.5cm and 3.2cm, respectively, and the remainder of the sound propagation was through fat tissue. The a density, thermal conductivity, perfusion rate, specific heat, acoustic coefficient, acoustic attenuation and speed of sound for this simulation can be seen in Table 3-1 in section 3 of this report.)

Sapareto and Dewey established an equation based on experimentation to quantify the amount of thermal energy applied to a volume of tissue (Sapareto S.A., 1984). This equation is given by

$$T_{43} = \int_0^t R^{43-T}\,dt \tag{1-3}$$

where: T_{43} = amount of time at 43°C to have same amount of thermal dose

$$R = \begin{cases} 0.5 \text{ if } T \le 43°C \\ 0.25 \text{ if } T > 43°C \end{cases}$$

T_{43} in equation 1-3 represents the amount of time tissues should remain at 43°C to have the same thermal energy applied at a given temperature, T, and exposure duration dt. This is defined as the thermal dose. The thermal dose is usually given in equivalent minutes (EM). A thermal dose of 240 EM is considered as the threshold for predicting lesion formation due to HIFU exposures (Damianou C., 1994).

The other major biological effect produced by HIFU is cavitation. Cavitation is the expansion, creation or distortion of a new surface within a liquid (Leighton T.G., 1994). In the case of tissues it is the distortion of micro bubbles already present within the tissue. There are two types of cavitation which are inertial and non-inertial. Non-inertial cavitation occurs when the bubbles inside of an acoustic wave absorb and scatter the acoustic wave (Leighton T.G., 1994). This type of cavitation causes the bubbles to expand and contract at an oscillating pattern. Non-inertial cavitation does not cause the collapse of the bubbles but can change the volume of

the bubbles within the tissue. The second type of cavitation is inertial cavitation. There are two phases to inertial cavitation which are the initial explosive growth and the collapse of the bubble (Leighton T.G., 1994). The initial explosive growth occurs just before the collapse of the bubble. This growth occurs during the rarefaction phase of the acoustic wave. The bubble reaches a maximum size and the compression phase of the acoustic wave halts its explosion. The bubble then attains a second maximum size during the next rarefaction phase of the acoustic wave and then collapses in the following compression phase. The pressures and temperatures that can be reached by this collapse can be between 1000 and 70 000 bars and 1000^oK to 20 000^oK (Flynn H.G., 1982). This rather explosive collapse takes place in a very small volume of a fraction of micrometers.

Cavitation occurs in any biological media which is in the presence of an acoustic field. Non-inertial cavitation occurs when the intensity of the acoustic field is relatively low. When the acoustic intensity is relatively high inertial cavitation occurs and the micro bubbles will rupture. This rupture causes irreversible tissue damage as it creates elevated temperatures and pressure (Curiel L., 2001).

Treatment of Prostate Cancer Using High Intensity Ultrasound

Transurethral Probes

Transurethral HIFU Probes

When the HIFU transducer is inserted into the urethra to ablate prostatic tissue they are considered a transurethral device. In this type of device there is usually no focusing of the ultrasound beam and the device is a flat surface that sends ultrasound which is mostly absorbed at the vicinity of the device. The ultrasound frequency is usually close to 8MHz in order to ensure enough heating of tissue close to the transducer (due to high attenuation of high frequencies). Different devices and procedures intended for the treatment of prostate cancer using transurethral high intensity ultrasound are currently undergoing their preliminary clinical testing (Chopra, R., 2009, Ross, A.B, 2004). For these referred approaches, MRI is used for guidance and temperature feedback.

The following types of devices and procedure were used for testing in the canine model. Ross *et al.* (2004) developed two types of transurethral probes one being a sector based array with 90° directivity and the other being a planar transducer array. Two sector based arrays were tested. Both arrays had an outer diameter of 3.5mm and length of 10mm. The two operating frequencies tested for these arrays were 8.6 and 8.3MHz. Two planar arrays were tested both of which had the same outer diameter and length as the sector based arrays. One of the planar arrays was tested with operating frequencies of 8.0 and 8.1MHz and the other was tested with operating frequency of 7.8MHz. Attached to the end of each device is a urinary retention bladder. After the device was inserted into the urethra the urinary retention bladder was inflated. MRI was then used to ensure that the active surface of the device was in the proper position. Surrounding the active surface of the transducer is a balloon filled with coolant liquid. A constant supply of degassed water flows within this balloon for cooling the device and for acoustic coupling between the transducer and the tissue. The device is then used to ablate tissue within the prostate with MRI thermometry feedback. This ablation was done by mechanically rotating the device to different locations of the prostate after the ablation of the current location is confirmed using

MRI thermometry. Both the sector based array and planar array were capable of ablating the canine prostatic tissue. The sector based arrays were less selective than the planar arrays, but required less rotation for treating treatment and therefore less treatment time. The planar arrays were more selective but required more treatment time to cover similar treatment regions as compared to the sector based array. This device is not focused which limits the treatment area selection.

Another transurethral probe intended for prostate treatment has been designed by Chopra *et al.* (2009) and it has been tested *in vivo* in the canine model. This device has only one surface element. The transducer of this probe is a flat element transducer that is 3.5mm x 15mm in surface area and has an operating frequency of 9.1 MHz. The acoustical energy produced by this device does not have a focal region. This device is intended for use in a guided intervention using MRI thermometry. The device consists of an MRI-compatible heating applicator, a rectal cooling device, an MRI-compatible rotational positioning system, cooling systems for circulating temperature-controlled water through the rectal and urethral devices, radio frequency electronics and hardware for ultrasound generation and motor control and computers and software interfaced with the MR imager for real-time processing of images and temperature maps during treatment. The acoustical power was controlled with input from the MRI thermometry feedback to control the temperature. This study successfully demonstrated the feasibility of using active MR temperature feedback with transurethral ultrasound therapy for targeted therapy of the prostate gland in the canine model. A different version of this device may soon be in clinical use under the company name Profound depending on the results of the clinical trials testing currently on going.

Trans-rectal Probes

Trans-rectal HIFU probes have been in commercial use for over a decade (reviewed in Kennedy J. E., 2005). The current HIFU trans-rectal treatment approaches ablate the entire prostate gland in order to destroy the malignant tissue. There are two commercially available trans-rectal HIFU systems; the Ablatherm[TM] (EDAP-TMS, Vaux-en-Velin, France) and the Sonablate®-500 (SB-500; Focus Surgery, Inc., IN, USA).

Ablatherm[TM] System

The original Ablatherm[TM] trans-rectal system shown in Figure 1-13 included a patient bed, a monitor to display the ultrasound image provided by a trans-rectal probe with a retractable imaging transducer and a treatment transducer. As shown in Figure 1-14, the treatment and the imaging transducer were independent and had to be switched between treatment and imaging modes during the therapy (Gelet, 1999). The transducer was a single-element device with a focal length of 40mm, a 50mm aperture which was truncated at 31mm and operated at 3MHz.

Figure 1-13. Ablatherm^{TM} HIFU Treatment Platform

Ablatherm^{TM} systems of this generation are currently being used in Europe, Asia, Canada and Mexico. At the beginning of the procedure, the patient is placed under spinal anesthesia to avoid movement during the procedure and an intravenous sedation to calm the patient as the treatment may last from two to three hours. A catheter is inserted into the prostatic urethra so that the procedure does not damage the urethra and to allow urination since the procedure causes swelling of the prostate. This catheter is typically removed after two weeks. The probe is coated with a gel wrapped with a latex condom that is filled with a cooling liquid and inserted into the rectum of the patient by an urologist using a robotic arm. An ultrasound imaging probe is used to locate the apex and the base of the prostate. Figure 1-14A shows an image of the imaging probe and treatment probe and Figure 1-14B shows the imaging transducer locating the apex region of the prostate.

A   **B**
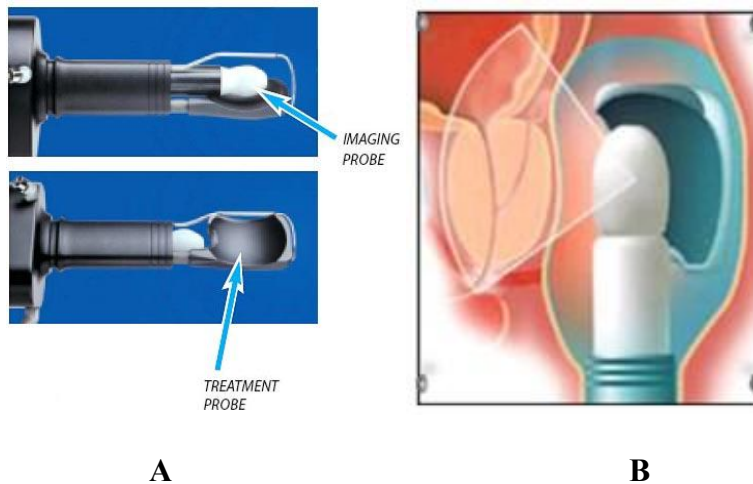
Figure 1-14. (A)Ablatherm^{TM} Trans-rectal Probe (B) Imaging Transducer Locating Apex of Prostate

The physician decides which regions to treat. The physician also specifies the rectal wall thickness as a security distance so that the rectum is not damaged. The probe is then switched to the exposure transducer. The transducer generates a series of high intensity ultrasound exposures of five seconds at each of the locations chosen by the operator followed by 5-s wait time between exposures. This allows enough time for the blood to remove heat between exposures and reduce the heat accumulation (Pichardo S., 2007).

At its first version, this treatment lacked real time imaging during the procedure. Pichardo *et al.* (2008) proposed an extension to this device in which the imaging device is permanently fixed to the center of the treatment transducer and not retracted during the treatment, (see Figure 1-15).

Figure 1-15. Real-time imaging probe. (Pichardo S., 2007)

This device can provide real time ultrasound imaging during the procedure. This device is now currently in use and some patients that were treated with this device were included in an outcome study for trans-rectal HIFU surgery. (Crouzet S., 2010). A clinical study using both versions of the Ablatherm^{TM} system showed comparable clinical outcomes. In this study, 803 patients from urological departments in Montpellier, Marseille, Lyon, Bordeaux, Nice and Toulouse France were treated with the first version (Ablatherm Maxis) or the second version (Pichardo S., 2008) of the Ablatherm system. The patients in this study were placed into D'Amico's risk groups based on the growth and spread of their prostate cancer. The bio-chemical free survival rate (BCFSR) was used to determine the effectiveness of the treatment. The BCFSR is a successive measurement of the PSA levels of a patient post operatively. The BFCSR after 7 years of the low, intermediate and high D'Amico risk groups in this study were 75%, 63% and 62% respectively. Patients with a significant increase in PSA levels, 182 patients in total, were considered to have failed in treatment and underwent hormonal or radiation therapy. In total 9 patients died from cancer related illness after 8 years.

Sonablate®-500 System

The other commercially available device is the Sonablate®-500. The Sonablate®-500 system consists of a coolant unit, a console for the operator, a flat screen monitor and a trans-rectal probe which contains two transducers (Illing R., 2006)(see Figure 1-16).

Figure 1-16. Sonablate®-500 System

The two transducers located in the trans-rectal probe are housed back to back and can have either a 3 cm or 4 cm focal length (Uchida T., 2006). The treatment procedure for the Sonablate®-500 is similar to that of the Ablatherm[TM]. The patient is first given spinal anesthesia and placed in a supine position with their legs open. The probe is inserted manually and placed under ultrasound imaging guidance facing the prostate. The probe is covered with a latex balloon and liquid is circulated to cool the device and provide acoustical coupling for the procedure. The prostate is then imaged at different planes from the base to the apex. The operator defines the treatment area and begins treatment at the apex of the gland and finishes at the base. Usually there are three defined sagittal sections for the treatment that are the anterior, mid-section and posterior sections seen in Figure 1-17 (Uchida T., 2006).
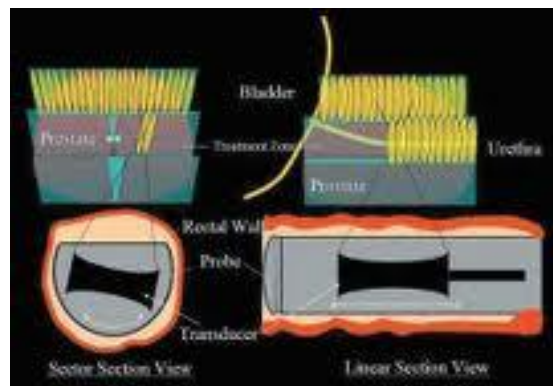
Figure 1-17 (Uchida T., 2006). Sagital treatment section for Sonablate®-500 HIFU surgery

A clinical outcome study was also conducted for the treatment of prostate cancer using the Sonablate®-500 system. (Uchida T., 2006). In this study 181 patients were treated with the Sonablate®-500 system. Hormonal therapy was required as a salvage therapy post HIFU for 52% of the patients. The patients in this study were also divided into D'Amico risk groups. The BCFSR after three years for the low, intermediate and high risk groups was 94%, 75% and 35% respectively. No patients died from cancer within five years after the treatment.

Morbidity

As for the other treatments discussed in this report there are possible complications from a trans-rectal HIFU procedure. The main complication for both the Ablatherm[TM] and the

Sonablate®-500 are partial or total loss of potency (%43.2 of patients). Other reported effects are stress incontinence (%5.7), urinary tract infections (%7.1), chronic or pelvic pain (%5.7) and less commonly rectourethral fistula (%2.20 (Uchida T., 2006, Poissonnier L., 2007, Rouviere O, 2007, Blana A., 2008). The most prevalent morbidity associated with trans-rectal HIFU surgery is the loss of potency (Rouviere O, 2007). The main reason for the loss of potency after a trans-rectal HIFU surgery is that a large percentage of the prostate is treated and the erectile nerves being close to the prostate they are most probably damaged during this procedure. Rectourethral fistulas are a rare but very severe complication of trans-rectal HIFU surgery as it requires major abdominal surgery. Netsch *et al.* (2011) conducted a study on this complication which included 363 consecutive patients whom underwent trans-rectal HIFU surgery using the Ablatherm[TM] Maxis device. Of these 363 patients 8 developed a rectourethral fistula. For both the Ablatherm[TM] and Sonablate®-500 systems multiple HIFU sessions are sometimes required for adequate treatment. Netsch *et al.* found that the occurrence of rectourethral fistula increases with the increasing number of HIFU sessions.

Section 2: Dual-modality Image Guided High Intensity Focused Ultrasound Device Design for Prostate Cancer: A Numerical Study

Motivation

The current treatment devices for trans-rectal HIFU ablate the entire prostate gland. This is mainly due to the fixed focal lengths of the devices. As previously mentioned in this report, there is an opportunity to reduce morbidity by limiting the treatment to a reduced area. In this numerical study, a new optimal HIFU device is proposed to locally treat tumor masses within the prostate while sparing surrounding structures and healthy prostatic tissue.

This new device is purposed to include dual-modality imaging capabilities: Magnetic Resonance Imaging (MRI) and Ultrasound Imaging (UI). A dual-mode imaging modality will allow complementing both modalities and exploring new alternatives for guidance. MRI is the only modality accepted by Federal Drug Administration in the USA to guide focused ultrasound surgery since it is able to measure temperature changes in the tissue (Hynynen K., 2010). Also, MRI-based techniques are exploring a much better localization of tumor masses in the prostate (Thoeny H.C., 2010) when compared to other imaging modalities. With standard UI, on the other hand, the effects of focused ultrasound on tissue are not clearly visible and tumor detection is not possible. However, new UI-based techniques are emerging where tissue elasticity properties are measured in real-time and these properties change under the effect of HIFU (Curiel L., 2009, Sapin-de Brosses E., 2010). These new UI techniques can provide, with a low-cost feedback, a control basis for HIFU treatment. Having a dual-modality imaging device will help to validate these new techniques against the established standard for guidance based on MRI. Also, the possibility of a complemented guidance can be considered where each modality can contribute in the treatment planning stages, real-time follow-up of effects and outcome assessment.

The technical challenge in the development of a new HIFU therapeutic device with dual-modality imaging implies that the device has to be MRI-compatible, which is ensured at fabrication stage, and include in its design the presence of an UI probe. The present study is concentrated in exploring the possibility of including this UI probe while offering the capability of targeting very precise regions in the prostate gland.

The device was first designed using simulation tools. The acoustic field produced by the device under idealized conditions was simulated and used to determine the optimal parameters required for the device. Then a model of the male pelvic region was created as the testing environment for the device. The treatment of simulated tumors within the prostate gland was conducted. The resulting acoustic field and heating pattern determined the feasibility of designing a device that can fulfill the needs for treatment.

Virtual Device Construction

Virtual construction of the device began with the choice of the shape of the therapeutic device. The overall shape was spherical to produce a natural focus. The device was designed to have the same truncated width, 31mm, diameter, 50mm, and central opening diameter, 25mm, as the latest Ablatherm^{TM} treatment probe (Pichardo S., 2008). The device was composed of concentric ring elements sub divided into independent elements. This is a combination of a spherical array and a sectorial array (Tan, 2001).

The surfaces of all of the elements of the transducer array were first virtually obtained in order to calculate the acoustic field.

Matlab was used to construct the data points which correlate to the surface of each element of the transducer using the following methodology which was used in Pichardo (2007). First two angles β and α were identified as seen if Figure 2-1A and Figure 2-1B. Angle β relates to the inner and outer edge of the transducer elements beginning from the edge of the central opening for lodging the imaging transducer and ending at the outer edge of the device respectively. Angle α relates to the radial edges of the device elements.

A   **B**
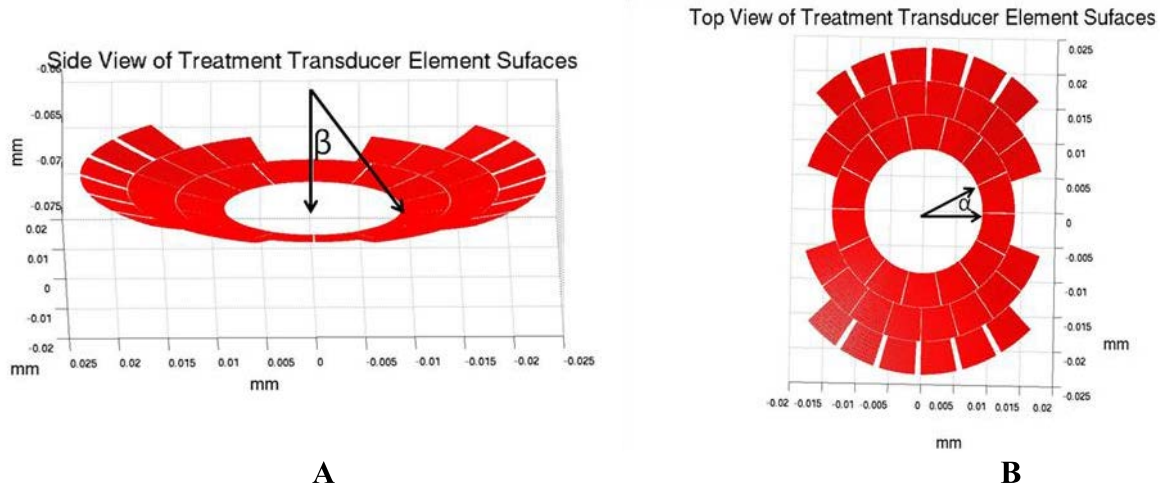
Figure 2-1. (A) Device Construction Side View (B) Device Construction Top View

By determining the angles β and α that corresponded to the corners of each element, the active surface area for the device was constructed as shown in an example in Figure 2-2. The elements of the treatment transducer were arranged in a ring configuration with each ring divided into same size sectional elements to enable dynamic focusing. The minimum distance between the edges of each element was set to $\lambda/4$. The elements of the transducer were then divided into smaller sub-elements for simulation using the Rayleigh integral. The complex velocity was first calculated to obtain the value of the acoustic pressure produced by the surface elements given by the Rayleigh-Sommerfeld diffraction integral (Fan X., 1992) given by

$$\varphi(r) = \frac{1}{2\pi} \int v_s \frac{e^{ikR-\alpha}}{R} ds \qquad (2\text{-}1)$$

$$p(r) = ikZ\varphi \qquad (2\text{-}2)$$

where: v_s = particle velocity on surface ds

$\alpha = R_1 * \alpha_1 + R_2 * \alpha_2 + R_3 * \alpha_3$ attenuation factor

R_1 = distance sound propagates in coolant liquid

R_2 = distance sound propagates in rectal wall

R_3 = remainder of distance sound propagates through (fat)

$R = R_1 + R_2 + R_3$

ds = surface area of selected element

$k = \frac{2\pi}{\lambda}$

Z = acoustic impedance of water

The surface elements used for the Rayleigh calculations had a width of $\lambda/4$. Figure 2-3 is an image of some of the array elements divided into surface elements used for calculations. By making these surface elements small compared to the distance at which the acoustic pressure is calculated and to the wavelength (λ) we can consider them as point acoustic sources, which is a criterion for the correct calculation of the Rayleigh integral.
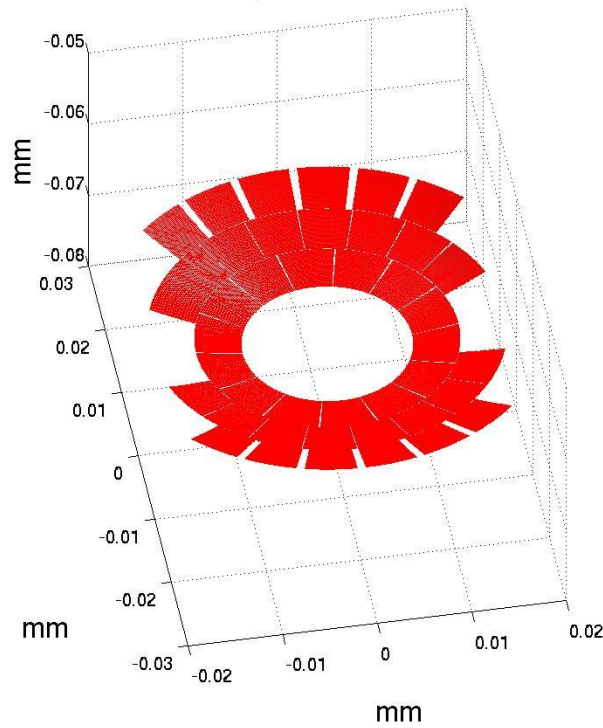
Figure 2-2. Example of Virtual Construction of Transducer
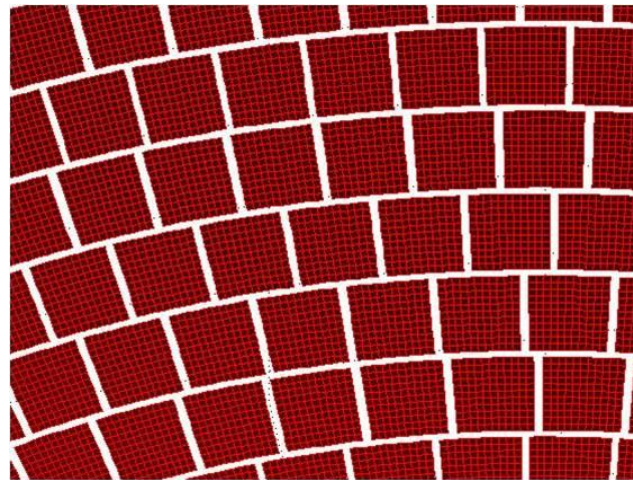
Figure 2-3.Close up of sub-elements

Digital Reconstruction of the Male Pelvic Organs

For proper modeling of the bio-effects induced by a transducer, the media in which the acoustic wave will be propagating through needs to be known. For the case of prostate cancer treatment the acoustic wave propagates through a coolant liquid, which is in the rectum, then the rectal wall, fat tissue and finally the prostatic tissue. Using the BHTE, the amount of heat generation can be estimated from the acoustic pressure and the thermal properties of the different types of tissue. The first challenge is modeling the distribution in the space of these thermal properties. For this, the size and location of all of the tissues in the male pelvic region have to be determined.

The size and location of the organs in the human male pelvic region were determined using full body histological images from the Visible Human Male Server Project (VHSMP, Ecole Polytechnique Federal de Lausanne, France). Images were downloaded and processed using the VHSMP interface (Figure 2-4A), which allows the user to see the region they are interested in. Figure 2-4B shows one of the images that were downloaded and that correspond to transverse slices of tissue at the male pelvis area. In total one hundred images with a resolution of 0.2 x 0.2 x 1mm, x,y,z respectively, were downloaded and analyzed.

A   B
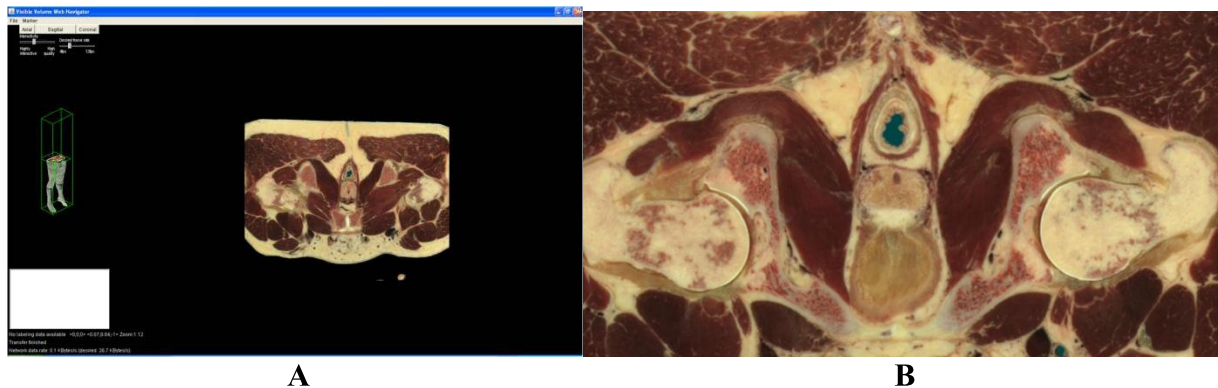
Figure 2-4. (A) Applet from VHSMP (B) An image downloaded from the VHSMP (http://visiblehuman.epfl.ch/)

For the image analysis a Graphic User Interface (GUI) was created in Matlab (Mathworks, Bethseda, MA, USA). Figure 2-5 shows the GUI Organ Volume Builder that was developed for this study and used for the analysis of the VHSMP images. The images from the VHSMP were loaded at the center of the GUI. The user of the GUI was capable of loading each of the images that were downloaded from the VHSMP. Once the user selected the desired image they could then choose the organ to create a mask for. The organs that were selected for labeling in this project were the prostate, the bladder, the rectum, muscular tissue, the ductus deferens, the seminal vesicles, the rectal wall, the rectal muscle and the nerve bundle. Any space that was not labeled was assumed to be fat. Confirming that the masks of each organ were created properly was done using an overlay displayed overtop the original image. Figure 2-6 illustrates an example where the masks for each organ are shown overlaying the original image.
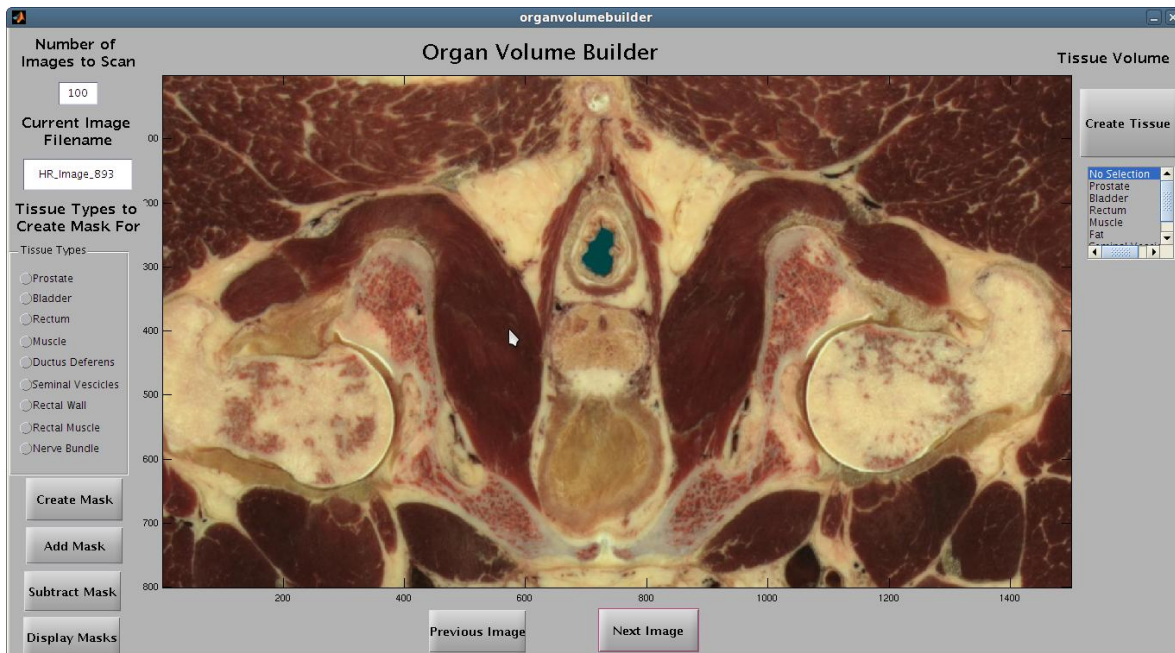
Figure 2-5. Organ Volume Builder GUI
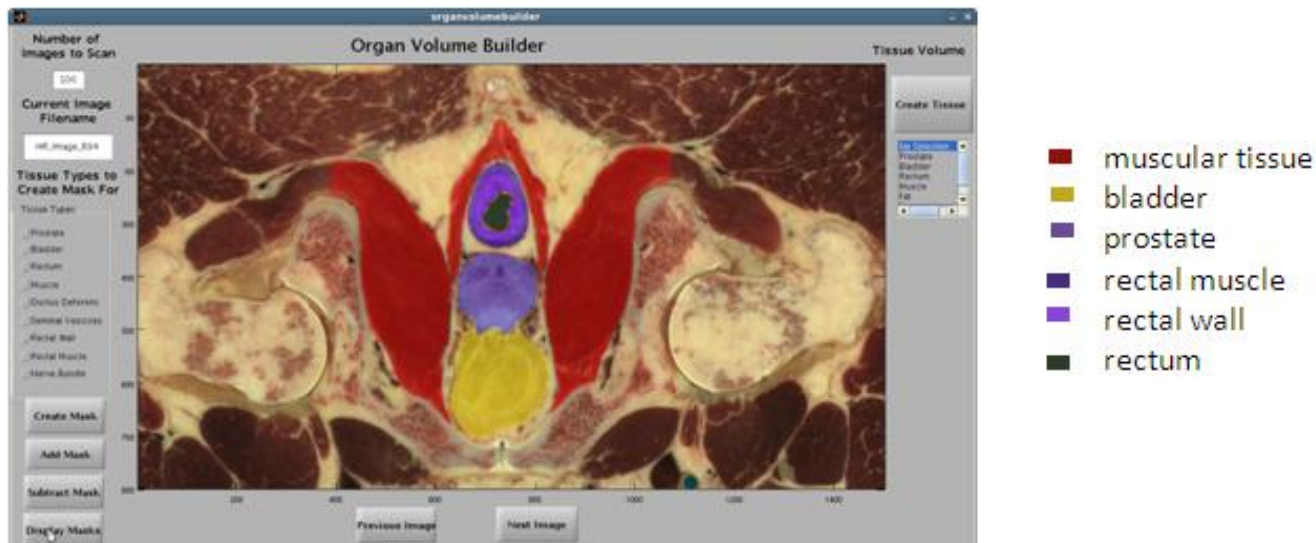
Figure 2-6. Image of masks produced by "Organ Volume Builder GUI"

In Figure 2-6 the yellow colored area is the mask of the bladder, the red area is the mask of the muscle tissue, the brown area is the rectum with the rectal wall and muscle in purple and blue respectively around it and the prostate gland in purple. The tissue between the prostate and the rectal wall is fat and was not labeled since all unlabelled space is assumed to be fat. If the user was not satisfied with the masks for the organs the software allowed for the revision of each slice of the masks. Once the user was satisfied with all of the masks for all of the selections they could then select the organ for which they wanted to create a volume for from the list box on the right side of Figure 2-6. Then the masks for each slice of the selected organ were combined into one mask and the organ was plotted in three dimensions as seen in Figure 2-7. The complete mask was then finished by using the "smooth3" Matlab function.

Figure 2-7. Unsmoothed Prostate

The smoothed prostate gland can be seen in Figure 2-8A. This was repeated for all of the organs listed previously and then only a region of interest surrounding the prostate gland was sub selected to produce Figure 2-8B which represents the tissue that will be considered for the simulation of the BHTE.

A   B
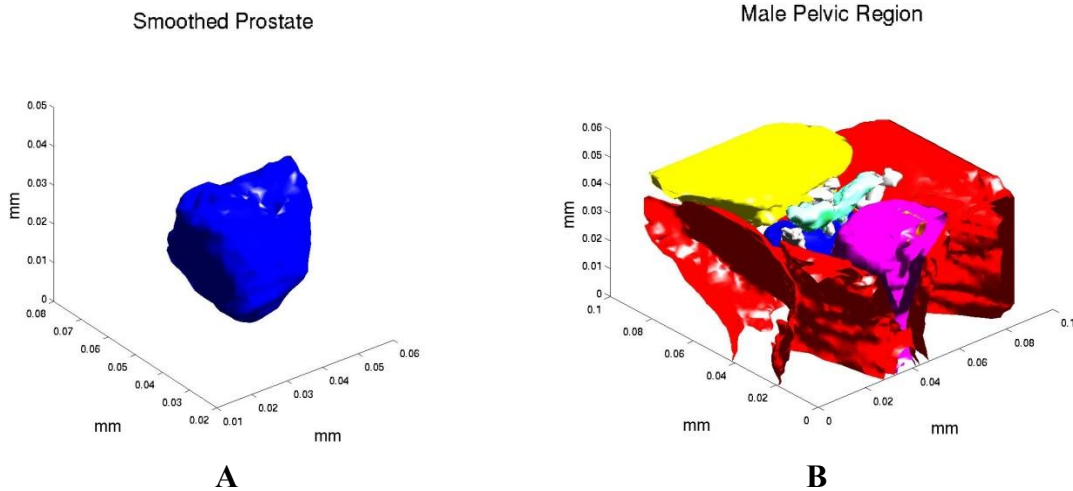
Figure 2-8. (A) Smoothed Prostate Gland (B) Region of Interest for Simulation

Parametric Numeric Study in Water-only Conditions

The diameter and truncated width of the device in this simulation were set to 50 and 31mm, respectively, as these dimensions are those of the currently used Abatherm[TM] device (Pichardo, 2008) and these parameters correlate to the anatomy of the rectum. The device included a central opening for an imaging probe for real time feedback of the treatment. The radius of the imaging central opening was set to 12.5mm to provide adequate space for lodging

the currently used imaging transducer in the Ablatherm[TM] system. Figure 2-9 is a schematic of the chosen fixed parameters for the initial water-only condition simulation.
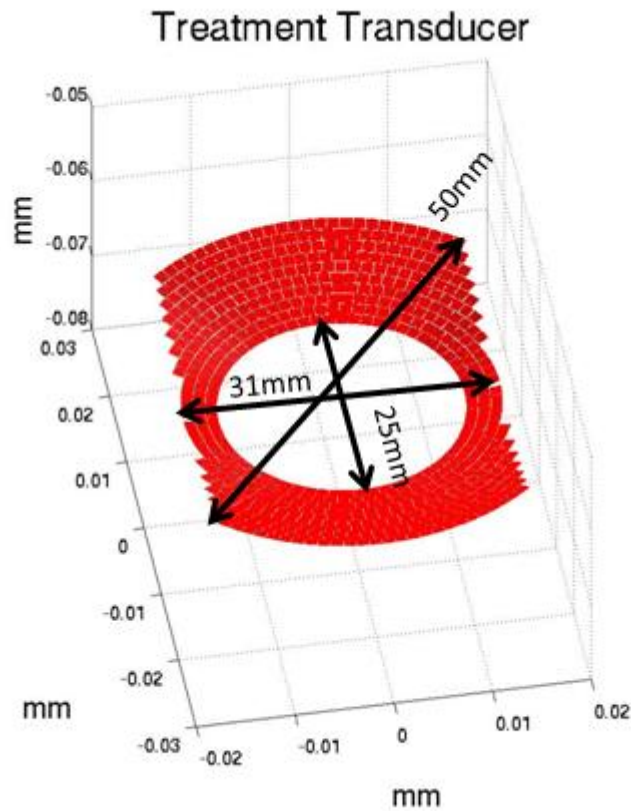
Figure 2-9. Schematic of therapeutic device

The operating frequency of the treatment transducer was set to 3MHz just as the Ablatherm[TM] treatment transducer to allow for the required treatment depth needed in this application.

Images from the VHSMP were used to determine the position of the center of the device relative to the posterior and anterior surfaces of the base, center and apex regions of the prostate. The transducer was centered to the rectum mask and the normal vector of the transducer was projected into the smoothed prostate at the apex, central and base regions. The transducer was then rotated at each region of the prostate for the entire width of the prostate in steps of 3°. The intersection of the normal vector and the smoothed prostate was calculated for both the anterior and posterior intersections for each angle of rotation at each section of the prostate gland. Figure 2-10 is an image of the intersection of the normal vector of the device intersecting with the smoothed prostate gland. The intersection is highlighted as a red triangle on the surface of the prostate gland. The maximum and minimum distance for the anterior and posterior intersections revealed the most extreme focusing distances from the surface of the device to the healthy prostate in the VHSMP. The intersections were found, relative form the center of the device, to be at 4.6 and 3.5cm for the apex, 6.5 and 3.1cm for the center, and 5.2 and 3.3cm for the base. These distances were used to determine the simulated HIFU treatment locations in the prostate and were chosen to be 2mm within the posterior and anterior limits of the prostate to safely test focusing at the boundaries. The calculated distances are summarized in Table 2-1. These test

41

point locations are similar to those found by Petrusca *et al.* (2009) for logical extreme acoustic test points in the prostate.
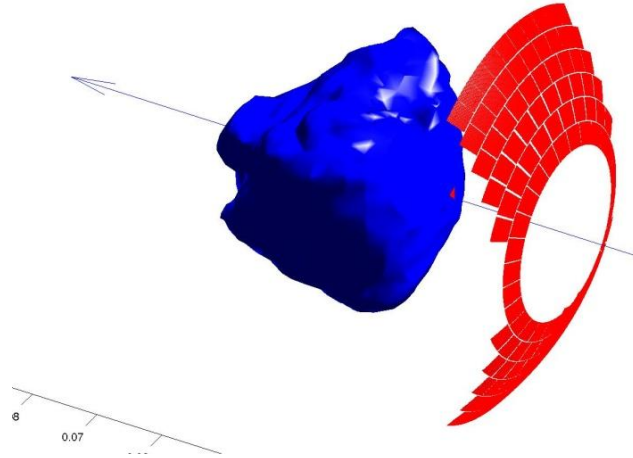
Figure 2-10. Intersection of Normal Vector of Transducer Array and Central Zone of Prostate Gland

Table 2-1. Treatment Locations for Simulation

Prostate Region	Posterior Distance (cm)	Anterior Distance (cm)
Base	3.5	5.0
Center	3.3	6.3
Apex	3.7	4.4

The initial acoustic simulation was performed with a single media condition using a cluster computer system consisting of 16 nodes each with two quad core Xeon 5405 processors. Water was chosen as the propagation media with a simulated acoustic attenuation of 2.88e-4Np/m/MHz (Hill C.R., 2004). The purpose of using water as the propagation media is that it has a very low acoustic attenuation and the calculations required for a single media are much simpler than those for multiple media. Therefore secondary lobes will be easier to find, as the sound will be less attenuated.

A parametric numerical study was performed to determine the optimal combination of focal length and elements size that would allow performing the desired focalization without appearance of secondary lobes.

The focal length was ranged from 45 to 60mm by steps of 1mm and the element size from 1λ to 8λ by steps of 0.5λ, where λ is the wavelength in water. In total 225 different combinations of focal length and element size were tested. The acoustic field was simulated using equations 2-1 and 2-2 (Rayleigh-Sommerfeld diffraction integral). The degree of focusing was quantified by the ratio of the pressure at the secondary lobe over the pressure at the primary lobe (η), given by

$$\eta = \frac{q_2}{q_1} \tag{2-3}$$

where: q_2 = acoustic pressure at the secondary lobe
q_1 = acoustic pressure at the primary lobe

The optimal device was chosen to be the configuration with the fewest elements and value of $\eta \leq 0.5$ for all focusing locations. The reason for choosing the configuration with the fewest elements is that devices with more elements are more expensive and difficult to construct, also each element will require its own amplifier and connection therefore more elements will add to the cost and complexity of the system. A device with $\eta \leq 0.5$ will have a main lobe twice the acoustic intensity of the secondary lobe. In a single media condition this will enable the device to produce a primary lobe at the target site without producing secondary lesions.

The parameters for the optimal device resulting from this study are summarized in Table 2-2. The optimal combination of focal length and element size was found to be 51mm and 3.1λ, respectively, producing a 358-element treatment device with a maximum η of 0.48. Having $\eta \leq 0.5$ means that this simulated device can achieve a focalization with a primary lobe twice its amplitude compared to that of the secondary lobe, and can therefore safely create a lesion without non-desired secondary lesions in the single media condition. These parameters will be used as the starting point for a more realistic simulation which will include the acoustic attenuation of the media in a transrectal HIFU prostate cancer procedure.

Table 2-2. Optimal Parameters for Water-only Condition Study

Parameter	Optimal Value
Highest Value of η	0.48
Operating Frequency	3MHz
Element Width	3.1λ
Focal Length	51mm
Truncated Width	31mm
Diameter	50mm
Central Opening Radius	12.5mm
Number of Elements	358

Focusing in the Pelvic Region

Trans-rectal HIFU treatment in reality is not performed in a solely water media condition. During this procedure the rectum is filled and distended by a cooling liquid (water solution). This action causes the rectal wall to distend. Therefore to create a more realistic simulation of an acoustic field created during a trans-rectal HIFU procedure the acoustic attenuation of cooling liquid, rectal wall and prostate need to be considered. A second simulation was performed to consider these acoustic conditions.

The first challenge in performing this simulation was to determine the distance the sound wave would propagate in each media. This was done by examining images from Pichardo *et al.* (2008) and the Ablatherm[TM] (EDAP-TMS, Vaux-en-Velin, France)) website which were produced by the imaging probe of the Ablatherm[TM] HIFU probe. Those images are seen in Figures 2-11A and 2-11B.

A   **B**

Figure 2-11. (A) Ultrasound image during a treatment obtained from Pichardo et. al. where A is the rectal wall, B is prostatic tissue and C is the urethra. (B) Images from the Ablatherm^{TM} website (Ablatherm^{TM}). The white spherical shape with a bulge in the middle is the therapeutic transducer and the centrally lodged imaging transducer. The red cigar shape is an image of the intended lesion which the transducer will produce during treatment. The distance marked by 3-8mm is the safety distance from the rectal wall to the prostate and the distance marked by 19-26mm is the length of the lesion inside of the prostate gland. The yellow arrows mark the distance from the rectal wall to the transducer surface.

Based on the images in Figure 2-11A and B, and the dimensions of the simulated transducer, it was determined that coolant liquid could be modeled as an elliptical cylinder with a major diameter of 3.9cm and a minor diameter of 2.6cm. The rectal wall thickness was then measured from the images acquired from the VHSMP and it was found to be approximately 0.6cm. This correlated to a distended rectal wall with an elliptical cylinder shape having a major diameter of 4.5cm and a minor diameter of 3.2cm. A three dimensional representation is seen in Figure 2-12 with the coolant ellipse (in brown), the rectal wall ellipse (in purple), the prostate (in blue) and the surface of the simulated transducer inside of the coolant liquid (in red).
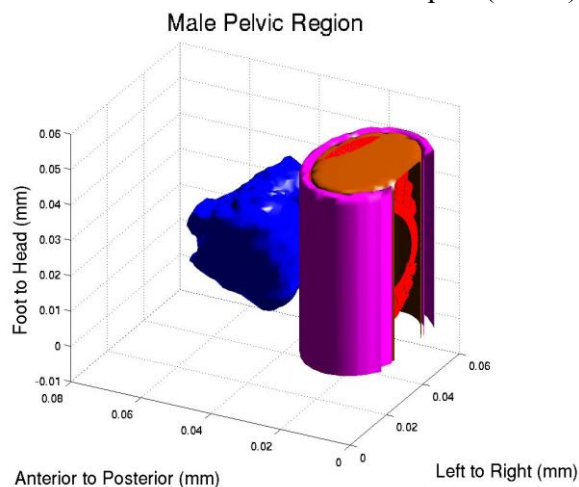
Figure 2-12. Image of the Coolant liquid (brown), distended rectum (purple), transducer (red) and the prostate (blue)

The initial calculation was to determine if all of the transducer elements were inside of the coolant ellipse. If this case was true then the acoustic field was calculated using the methodology

explained previously using 2-1 and 2-2. The acoustic attenuation of each media was incorporated into (2-1) as α. The values of acoustic attenuation were used for each the media in the simulation are shown in Table 2-3. These values are from previous simulation work (Pichardo S., 2008). The rectal wall acoustic attenuation used is the same as that for muscle as the rectal wall is a muscular tissue.

Table 2-3. Acoustic Attenuation of Media

Media	Acoustic Attenuation (Np/m/MHz)
Prostate	9.0
Rectal Wall	4.1
Coolant Liquid (water)	2.88e-4

The multiple media simulation was performed using two graphics processors (NVIDIA Tesla C1060) instead of the cluster used for the first simulation. For a more detailed description of the implementation of the GPU resource please see the *acoustic field calculation algorithm* section of the appendix. The graphics processors were used because they are less expensive and were capable of running the simulation approximately %60 faster than the cluster. The program was developed in both Matlab and Computer Unified Device Architecture (CUDA). The Matlab version was used for quality assessment of the CUDA version. The average percent error between the Matlab and CUDA programs obtained at 40 test points was %0.05 for the calculated acoustic pressure magnitude and %0.0027 for the phase of the acoustic field.

As in the first simulation in water conditions the frequency was set to 3MHz, the diameter and truncated width of the device were set to 50 and 31mm, respectively, and there was a central opening in the middle of the device to lodge the imaging transducer with a radius of 12.5mm. The parameters used for this simulation were a focal length ranging from 50mm to 60mm by steps of 1mm and the element size from 1.5 λ to 3.5λ by steps of 0.2λ. The total number of simulations was 100.

After completion of this simulation it was apparent that focusing at the farthest treatment area was not possible with this configuration. There was no combination of parameters that met the $\eta \leq 0.5$ criterion. Figure 2-13 is a three dimensional representation of the 6 dB level of the acoustic field in red and the surface area of the transducer. The transducer in this image has a focal Length of 60mm, element width of 1.5λ, a central opening radius of 12.5mm and is intended to focus at a treatment location that is 6.3cm away from the center of the transducer. This particular configuration has the furthest natural focus and the smallest element size and it should be the best at focusing at the furthest treatment location. However, as seen in Figure 2-13, there are secondary lobes located far before the desired treatment location. This would result in secondary lesion and is not an acceptable outcome for a treatment system.

Poor Focus with 1300 Elements
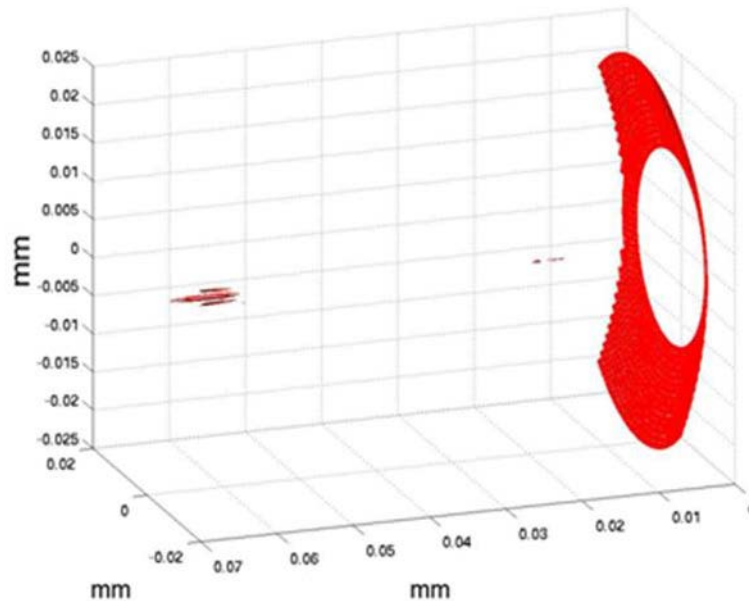
Figure 2-13. Three dimensional image of Acoustic Field intensity greater than 6dB.

Possible solutions for the problem of the degree of focusing included increasing the natural focal length of the device past what was previously tested, decreasing the frequency, increasing the device diameter and decreasing the radius of the central opening.

Increasing the focus past what was previously tested may result in better focusing at distances farther from the device as determined by Pichardo *et al.* (2009). Decreasing the frequency would result in better penetration of the sound waves. Increasing the diameter of the device would allow for more elements to be added to the device. Decreasing the central opening radius would enable the transducer to have more elements. The issue with decreasing the central opening radius was that the imaging transducer intended for this device has a radius of 12.5mm and a smaller radius would mean a new ultrasound imaging probe would be required. Each of these propositions was tested to see if the desired degree of focusing could be achieved.

Increasing the Device Focus

In this simulation the focal length of the device was ranged from 61mm to 75mm by 1mm steps and the element width was ranged from 1.5λ to 3.5λ by steps of 0.2λ. The frequency was set to 3MHz, the diameter and truncated width of the device was set to 50 and 31mm, respectively, and the radius of the central opening to lodge the imaging transducer was set to 12.5mm. The total number of simulations was 140. The optimal degree of focusing was achieved for a focal length of 68mm with an element width of 2.1λ. The parameters for the optimal device resulting from this study are summarized in Table 2-4.

Table 2-4. Optimal Parameters for Increasing Device Focus Study

Parameter	Optimal Value
Highest Value of η	0.58
Operating Frequency	3MHz
Element Width	2.1λ
Focal Length	68mm
Truncated Width	31mm
Diameter	50mm
Central Opening Radius	12.5mm
Total Elements	707

An acceptable degree of focusing, $\eta \leq 0.5$, could not be achieved for all treatment locations for any configuration. Therefore there was no configuration with these parameters that provided a sufficient degree of focusing. The best focusing was achieved for a device focal length of 68mm.

Varying the Frequency

The next simulation was performed to see if decreasing the frequency would increase the degree of focusing at farther treatment locations within the body. The reasoning behind this decision is explained by Cobbold (Cobbold R.S.C, 2007) in equations 2-4 and 2-5.

$$I(x) = I_o e^{-2\alpha x} \tag{2-4}$$
$$\alpha = \alpha_o f^n \tag{2-5}$$

where: x = distance (cm)

$\qquad f$ = operating frequency (MHz)

$\qquad \alpha_o$ = temperature dependent factor (Np/cm*MHz^2)

$\qquad 1 < n < 2$

It can be seen from equations 2-4 and 2-5 that the distance is inversely related to the operating frequency of the device. Therefore decreasing the frequency should increase the acoustic intensity at a farther location within the body. Based on this theory the simulation was performed again with a frequency range from 2.25MHz to 2.75MHz in steps of 0.25MHz with a focal length of 68mm, a central opening radius of 12.5mm and element widths ranging from 1.5λ to 2.3λ by steps of 0.2λ. The optimal operating frequency based on the results of this simulation was found to be 2.75MHz. The parameters for the optimal device resulting from this study are summarized in Table 2-5.

Table 2-5. Optimal Parameters for Varying the Frequency Study

Parameter	Optimal Value
Highest Value of η	0.58
Operating Frequency	2.75MHz
Element Width	2.1λ
Focal Length	68mm
Truncated Width	31mm
Diameter	50mm
Central Opening Radius	12.5mm
Number of Elements	590

An acceptable degree of focusing, $\eta \leq 0.5$, was not achieved for all of the treatment locations with the same configuration. The best compromise for degree of focusing was achieved with an element width of 2.1λ and an operating frequency of 2.75MHz.

Varying Device Diameter

The purpose of this simulation was to determine if increasing or decreasing the device diameter provided a major benefit to the degree of focusing of the device. If the larger device diameter permitted a better degree of focusing then further research would be required to determine the compatibility of this device and the anatomy of the rectum. Increasing the diameter of the device allows for the addition of more transducer surface without affecting the central opening size for lodging the imaging transducer. This simulation was produced using diameters of 40mm and 60mm diameter with a focal length of 68mm, an operating frequency of 2.75MHz, a truncated width of 31mm and element widths ranging from 1.5λ to 2.3λ in steps 0.2λ. The best compromise from this simulation was a device with a diameter of 60mm and an element width of 2.1λ. The parameters for the optimal device resulting from this study are summarized in Table 2-6.

Table 2-6. Optimal Parameters for Varying the Device Diameter Study

Parameter	Optimal Value
Highest Value of η	0.53
Operating Frequency	2.75MHz
Element Width	2.1λ
Focal Length	68mm
Truncated Width	31mm
Diameter	60mm
Central Opening Radius	12.5mm
Number of Elements	792

This simulation also demonstrated that the desired degree of focusing could not be reached with this given configuration.

Decreasing the Central opening Radius

Decreasing the central opening radius was not the desired design change to achieve an acceptable degree of focusing as this would lead to no longer being able to lodge the 12.5mm wide imaging transducer.

We first set the frequency to 2.75MHz and the focal length to 68mm since those were the values closest to a successful configuration obtained from the previous results. The central opening radius was then ranged from 1mm to 11mm by steps of 2mm and the element width was ranged from 1.7λ to 2.3λ in steps of 0.2λ. The optimal parameters for a device in this simulation was found to be a device with a focal length of 68mm, an operating frequency of 2.75MHz , an element width between 2.0λ and 2.2λ with a maximum central opening radius of 9mm.

To more accurately determine the optimal parameters a second simulation was performed with the same parameters as the central opening radius simulation except the element width was ranged from 2.0λ to 2.2λ by steps of 0.05λ. The parameters for the optimal device resulting from this study are summarized in Table 2-7.

Table 2-7. Optimal Parameters for Decreasing the Central Opening Radius Study

Parameter	Optimal Value
Highest Value of η	0.49
Operating Frequency	2.75MHz
Element Width	2.05λ
Focal Length	68mm
Truncated Width	31mm
Diameter	60mm
Central Opening Radius	9mm
Number of Elements	761

In Table 2-7 it can be seen that at an element width of 2.05λ the maximum $\eta = 0.49$. The optimal device parameters for the simulation were a focal length of 68mm, an operating frequency of 2.75MHz, a diameter of 50mm, truncated width of 31mm, an element width of 2.05λ and a central opening radius of 9mm. This configuration will be studied in further detail to determine if it is capable of treating tumors within the prostate, particularly if it is capable of steering the focus to acceptable distances.

Steering Capabilities

The location of a tumors in the prostate gland will not necessarily be on a normal vector from the device center, therefore electrical dynamic focusing must be used to steer the location of the focal zone in the lateral (left to right), vertical (head to foot) and axial (anterior to posterior) directions. Figure 2-14 is an indication of the lateral, vertical and axial direction in reference to the prostate (blue), the distended rectum (purple) and the transducer (red).
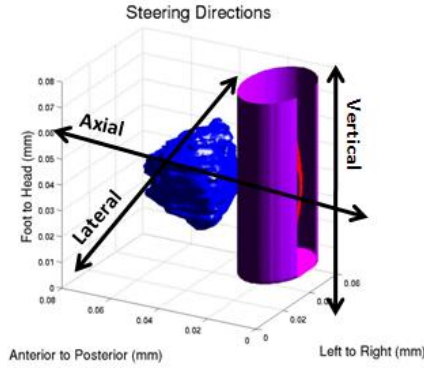
Figure 2-14. Steering directions for prostate treatment. Prostate in blue, distended rectum in purple and transducer in red.

Steering the focal zone in the axial direction has already been tested in the previous simulations by choosing points that were between 3.3 and 6.3cm from the center of the device. To determine how well the focal point could be steered in the other directions the problem was divided into two parts. The first was to determine the amount of lateral steering capable at each of the chosen treatment distances. The second was to determine the maximum vertical steering capable at each of the axial treatment locations. The value of $\eta \leq 0.5$ was again used to evaluate the degree of focusing. The maximum lateral and vertical steering capabilities for the chosen optimal device configuration (focal length of 68mm, operating frequency of 2.75MHz, diameter of 50mm, truncated width of 31mm, element width of 2.05λ and a central opening radius of 9mm) is summarized in Table 2-8.

Table 2-8. Steering Capabilities of Concentric Ring Array

Axial Treatment Distance (cm)	Maximum Lateral Steering (mm)	Maximum Vertical Steering (mm)
3.3	12.75	16.50
3.5	13.00	15.50
3.7	13.00	15.50
4.4	12.00	13.50
5.0	11.75	3.00
6.3	5.75	0.50

Randomly Placed Array Comparison

As discussed earlier in this report the spacing between elements centers in an array needs to be less than the wavelength of the signal being transmitted to eliminate the first grating lobe (see equation 1-1). Another potential solution to avoid grating lobes is to randomly place the transducer elements on the surface of the device. Randomly distributed arrays can produce a non uniform distribution of the acoustic field produced by the group of independent elements. This results in less constructive wave summation in the pre-focal region and hence fewer grating lobes.

The possibility of the random array to produce a better degree of focusing was simulated. Independent circular transducer elements were placed on the excitation surface of the transducer

using a pseudorandom pattern calculated with the function "random" of Matlab. As in previous simulations these elements were sub-divided into smaller surface elements of size $\lambda/4$. Figure 2-15A is an image of one of the circular independent elements that were created to simulate the randomly placed elements on the truncated array. In total ten attempts were made to create an array with the most possible number of independent circular elements. Table 2-9 gives the total number of randomly positioned elements on the surface of the transducer at each attempt. Each transducer had a focal length of 68mm, truncated at 31mm, a diameter of 50mm, an operating frequency of 2.75MHz, a central opening at its center with a 9mm radius and an element size of 2.05 λ. The maximum number of randomly placed elements on the device surface was 535, with a minimum distance between the edges of independent elements being $\lambda/4$. Figure 2-15B is a three dimensional image of the transducer that was simulated.

A   **B**
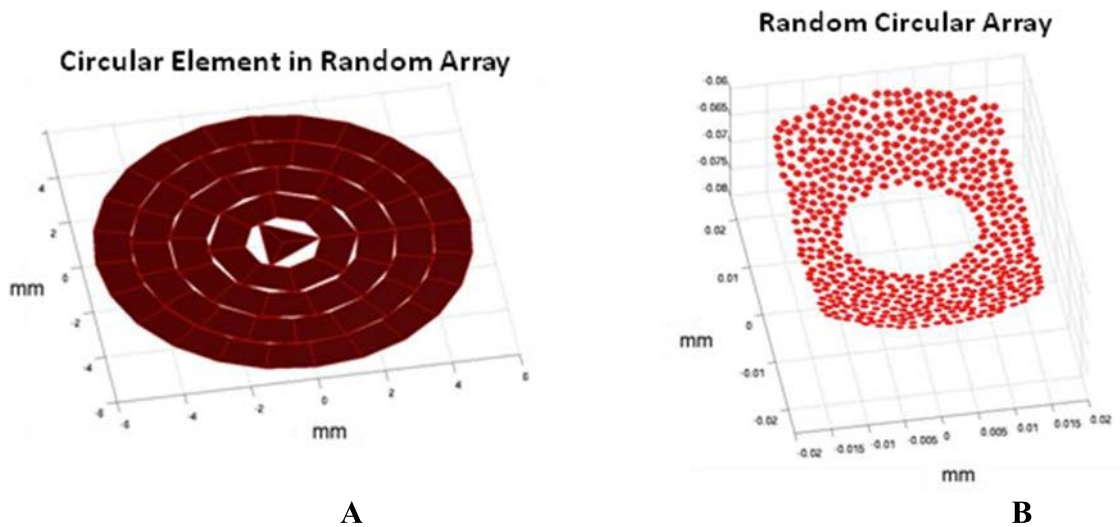
Figure 2-15. (A) Independent element with Sub-elements (B) Complete transducer with randomly placed elements.

Table 2-9. Number of Elements Randomly Produced

Attempt Number	Number of Randomly Placed Elements
1	520
2	530
3	526
4	520
5	**535**
6	523
7	521
8	521
9	517
10	526

The transducer with 535 elements was then tested at each of the treatment zones discussed earlier using the same software that was developed for the multiple media simulation. An acceptable

degree of focusing was achievable with the randomly distributed array produced in this simulation along the normal axis of the array with a maximum $\eta = 0.49$.

Steering the Random Array

To test the beam steering ability of the random array steering in both the negative and positive direction of each steering axis had to be examined. The reason for testing both directions is that due to the lack of geometrical symmetry it is possible that one direction has a better steering than the other. Table 2-10 is a summary of the lateral and vertical steering achieved for both the negative and positive direction.

Table 2-10. Steering Capability of Random Circle Array

Treatment Distance (cm)	Maximum Lateral Steering (mm)	Maximum Vertical Steering (mm)
3.23	$\pm$16.00	$\pm$10.50
3.5	$\pm$16.00	$\pm$8.50
3.7	$\pm$16.00	$\pm$7.50
4.4	$\pm$15.5	$\pm$2.00
5.0	$\pm$10.00	$\pm$0.50
6.3	0.00	0.00

In Table 2-10 it can be seen that the randomly distributed circular element array can steer slightly farther away from the transducer central axis in the lateral direction than the concentric subdivided elements array at closer points to the transducer surface. However the randomly distributed circular element array cannot steer the focal region at the farthest treatment location (6.3cm). Also the concentric ring array was superior in steering in the vertical direction at all treatment distances. Therefore treatment with the randomly distributed circular element array would require more mechanical displacement to produce the same degree of focusing as the concentric subdivided elements array. Also the total active surface area is less in this configuration and will require a higher acoustic surface intensity for each element to produce the same amount of acoustic energy at the treatment site.

Random Element Excitation

As was seen in the Steering the Random Array simulation the random distribution enabled better steering of the acoustic field at test points closer to the device, but the random circular array of elements was unable to achieve the appropriate degree of focus for the furthest treatment location (6.3cm). Another idea that was explored for lowering the grating lobes due to concentric element design was to randomly excite elements within the concentric subdivided circle array. The phase of each element in the concentric subdivided elements array was calculated for the given test point. Then elements were randomly chosen to be excited for the treatment. Figure 2-16 is a three dimensional image of 512 randomly chosen elements. The red elements in Figure 2-16 were inactive for the simulation and the blue elements were the excited for therapy. The excited elements of the transducer array are colored in blue in Figure 2-16.
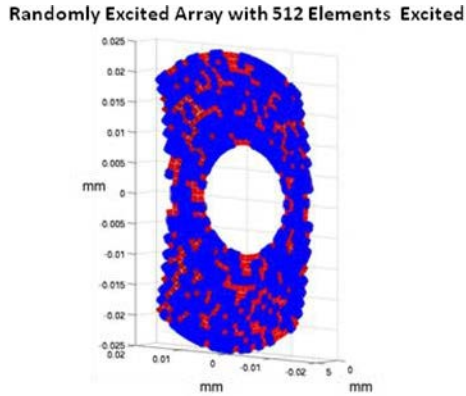
Figure 2-16. Random Excitation of Elements in Concentric Subdivided Circles Array
(excited elements in blue, inactive elements in red)

Table 2-11 has the information regarding the number of elements excited and if the degree of focusing was reached. It can be seen in Table 2-11 that an acceptable degree of focusing was only achieved when all of the elements in the array were excited. This means there is no possible random excitation which can produce a better degree of focusing than exciting all of the elements.

Table 2-11. Focus achieved for the Number of Elements Excited in the Concentric Subdivided Circles Array

Number of Randomly Excited Elements	Degree of Focusing Reached ($\eta \leq 0.5$)
512	No
550	No
600	No
650	No
700	No
750	No
755	No
761	Yes

Acoustic Simulation Discussion

The acoustic simulation used to determine the optimal device was conducted for a number of different configurations of the focal length, element size, operating frequency and central opening radius. The optimal device found in this study for the dual modality prostate cancer treatment device was a concentric ring array with a **focal length of 68mm, an operating frequency of 2.75MHz, a diameter of 50mm, a truncated width of 31mm, an element width of 2.05λ and a central opening radius of 9mm**. Although the current imaging transducer used in the Ablatherm[TM] system would not fit in this central opening there are other potential solutions for real time ultrasound imaging. Those possible solutions will be introduced in the discussion section of this report.

As well, the random circular array and randomly excited elements on the concentric ring array were tested to determine if these devices could enable the degree of focusing required for

treatment. The reason for randomizing the placement of the elements was to reduce the constructive wave interference at locations that were not at the desired focal region. This type of device did not perform as well as the concentric ring array as it has less active element surface area and was unable to steer the acoustic field to all the desired locations.

The randomly excited simulation was tested to try to reduce the constructive wave interference at locations applying the same theory that was purposed for the randomly placed circular array. It was hypothesized that a random selection of elements could reduce the undesired constructive interference whilst providing the degree of focus required for treatment. This simulation also did not meet the focusing requirements for a treatment device.

The optimal focal length for focusing at all of the regions previously defined was 68mm. This focal length is well past the intended target range of 3.3cm to 6.3cm. Similar results were found by Pichardo *et. al* (2009) when simulating the treatment of atrial fibrillation in the heart using a similar device.

In this simulation it was also observed that farther from the center of the device the treatment locations were, the larger the region at -6dB were in the axial direction. Figure 2-17 is an isosurface image at -6dB of the different acoustic fields produced at 3.3, 3.5, 3.7, 4.4, 5.0 and 6.3cm respectively.
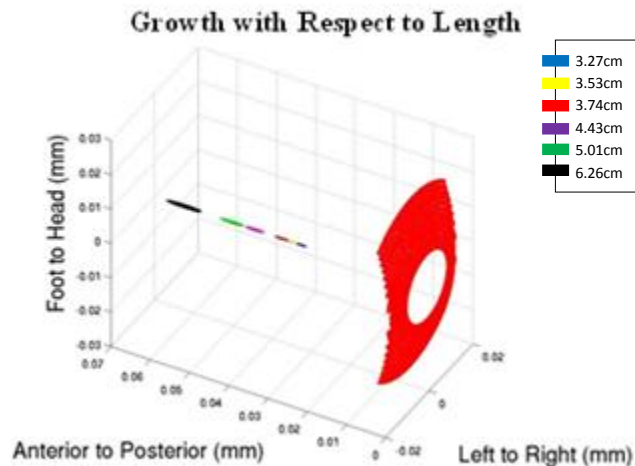
Figure 2-17. -6dB region growth with respect to distance from the transducer

This -6dBgrowth relative to treatment location distance from the transducer is occurring because the acoustic field is less focused at farther distances. The natural focus of this device produces an elliptical focal region, which becomes less focused and therefore extends in the axial region when treatment locations are chosen farther away from the device center.

Increasing the device diameter in this simulation did not improve the degree of focusing as well when compared to decreasing the central opening radius, even if both scenarios increased the surface area of the device.

The GUI developed in this project was crucial in the creation of the multiple media testing environment. By downloading images from the VHSMP the user was able to select specific anatomical regions and organs in the body for modeling. This software gives the user complete freedom to develop their tissue data set and tailor it to their specific requirements. Future users of this software could use it to create tissue data for conducting HIFU simulations in different regions of the body such as the heart, liver kidneys, or to make data sets for other experimental simulation that do not use HIFU.

54

Section 3: Thermal Lesion Simulation

Purpose

The expected biological effects from applying acoustic energy during a HIFU procedure within the male pelvis were estimated using the BHTE and the thermal dose concept (Sapareto S.A., 1984). However, before the thermal lesion simulation could be performed, relevant treatment locations were chosen for treatment of prostate cancer. Tumors were defined at different treatment locations within the modeled prostate from the VHSMP images.

Tumor and Test Point Selection

A literature review was done to determine the proper location and size of tumors for testing the efficiency of the designed device to produce the desired thermal effects for an effective treatment. Coakley *et al.* (2002) performed a study intended to determine prostate cancer tumor volumes using an endorectal coil for magnetic resonance spectroscopy imaging. In this study 37 patients were imaged and the location and volume of the tumors were estimated from the MRI images. After the imaging, the patients underwent a radical prostatectomy and a pathologist examined the patients removed organs. In total, fifty eight tumor nodules were found. Nineteen patients had a single nodule, fifteen patients had 2 nodules and three patients had 3 nodules. Fifty one tumor nodules were found in the peripheral zone and seven were found in the transitional zone. The minimum, maximum and mean tumor volumes for the tumor nodules found in the peripheral zone of the examined prostates were 0.02cc, 3.70cc, and 0.79cc respectively. The minimum, maximum and mean tumor volumes for the tumor nodules found in the transitional zone of the examined prostates were 0.04cc, 2.70cc, and 0.80cc respectively.

The tumor nodule sizes that were chosen for both the transitional and peripheral zone were the minimum, mean and maximum for each zone. For simplicity the tumor shapes were all considered to be ellipsoid. Figures 3-1A, B, C, D, E and F are three dimensional images of the tumors that were used in the thermal simulation. The tumors are shown in black and the prostate gland is shown in blue. Initially all of the ellipsoid tumors were chosen to have their major axis be in the left to right direction, but once they were modeled it was apparent that this would create test points in locations too similar to be of any relevance to the study. Therefore tumors 2 and 5 were rotated and aligned as close to the prostatic capsule as possible to give a larger variance in the treatment locations and to test if heating close to the capsule edge was possible without damaging surrounding organs.
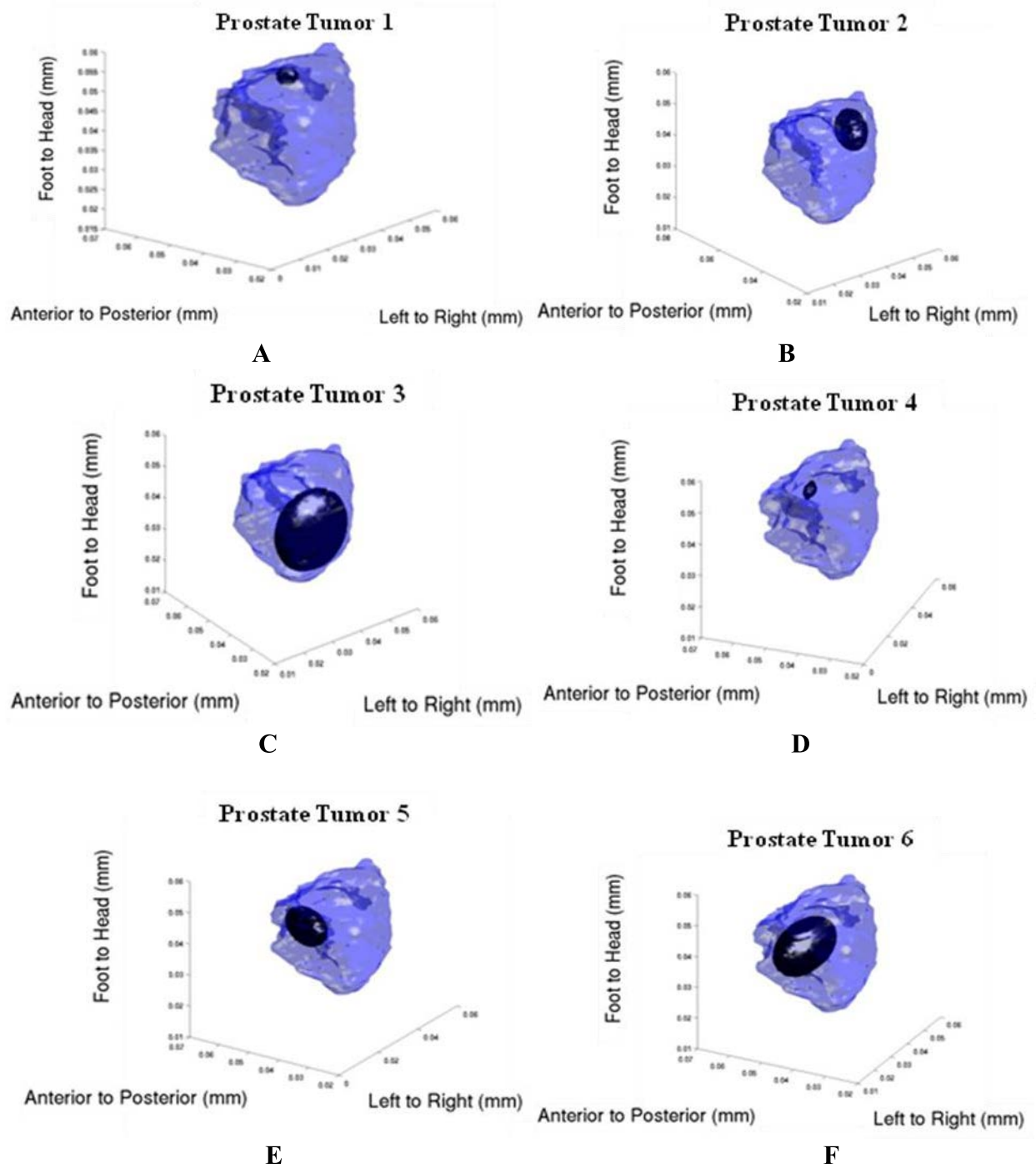
Figures 3-1 A, B and C are tumors in the peripheral zone of volume 0.02cc, 0.79cc and 3.70cc respectively. Figures 3-1 D, E and F are tumors in the transitional zone of volume 0.04cc, 0.8cc and 2.70cc respectively.

In this simulation we plan to test the capability of the designed device to ablate cancerous prostatic tissue without affecting surrounding organs and healthy tissue. The transducer center will be aligned with the tumor centers to test the lateral and axial steering. Therefore test points

were defined as the axial and lateral limits of the tumors. These points were chosen because they will be the locations that are still part of the tumor but are closest to surrounding organs and healthy prostatic tissue. Besides, treating at the lateral and axial limits will be the most challenging since they are the farthest points from the center of the device, therefore adequate focusing at these locations is the most difficult to achieve.

Bio-Heat Transfer Equation

As discussed earlier, the Bio-Heat Transfer Equation (BHTE) can be used for calculating the heating effects on biological tissue. For this study, the BHTE (3-1), was implemented using the numerical Finite Difference Time Difference technique defined by Yin *et al.* (2006) and calculations were performed using two graphics processors (NVIDIA Tesla C1060). For a more detailed description of the implementation of the GPU resource please see the *BHTE calculation algorithm* section of the appendix. Boundary conditions at the borders of the tissue volume were set to body temperature (37C). The discretization of the BHTE was implemented using a finite-difference scheme. The BHTE calculation requires a number of tissue, thermo-mechanic and biological properties including the tissue density (ρ), thermal conductivity (K), perfusion rate (ω), specific heat (C), attenuation coefficient (ι), acoustic absorption coefficient (χ) and the speed of sound (c) in each tissue.

$$\rho_t C_t \frac{\partial T_P(x,y,z,t)}{\partial t} = K_t \nabla^2 T_p + \omega_s C_s \left[T_s - T_p \right] + Q_p \qquad (3\text{-}1)$$

Also the specific heat and density of blood is required for the BHTE calculation. Table 3-1 shows the values for each tissue properties used in the Thermal Simulation.

Table 3-1. Tissue Properties used for Thermal Simulation

Property	Fat	Muscle	Bladder	Ductus Deferens	Seminal Vescicles	Prostate	Nerve Bundle	Rectal Wall	Coolant Liquid
Density (ρ)(kg/m^3)	916	1041	1040	916	916	1045	1038	1041	1000
Thermal Conductivity (K) (W/m/K)	0.248	0.4975	0.248	0.248	0.248	0.537	0.248	0.4975	0.5867
Perfusion Rate (ω) (mL/kg/min)	28	38	28	28	28	100	28	38	0
Specific Heat (C)(J*kg/K)	2490	3620	2490	2490	2490	3620	2490	3620	4180
ι (Np/m/MHz)	7.0	7.6	9.3	9.3	9.3	9	12.9	4.1	2.88e-4
χ	0.85	0.85	0.85	0.85	0.85	0.85	0.85	0.85	1
c (m/s)	1430	1572	1430	1430	1430	1572	1615	1572	1500

Blood	Specific Heat: 3840 J*Kg/K	Density: 1060 Kg/m^3

Values from Table 3-1 are from Duck F.A., 1990, Pichardo S., 2009, Pichardo S., 2008 and Bamber J.C., 1979.

During the trans-rectal HIFU procedure coolant liquid circulates within a balloon surrounding the device, therefore the properties for the coolant liquid are also required for the simulation and are also shown in Table 3-1. The circulation of this liquid changes the initial temperature of the male pelvis region pre-HIFU treatment. As it cools the device it also cools the rectum and surrounding tissue. The effect of this cooling was simulated in the BHTE as a boundary condition using a Newtonian flux convention (Pichardo, 2007).

Typically the core temperature of the human body is 37°C (Freedberg I.M, 1999) and the ideal temperature of the coolant liquid in the rectum is 13°C. Therefore the initial temperature for all tissues was set to 37°C and the initial temperature of the coolant liquid was set to 13°C. The BHTE program was run on the graphic processors (NVIDIA Tesla C1060) in succession until the maximum temperature difference between each point from the previous iteration as compared to the current iteration was less 0.01°C. Having a maximum temperature difference of less than 0.01°C between iterations meant that the tissues had reached their steady temperature and the cooling effects of the coolant liquid had reached completion.

Lesion Prediction

The simulation of the thermal effects from HIFU treatment was performed for two test locations at the axial and lateral limits of each modeled tumor. The device center was aligned with the center of each tumor. Tissues that had reached a T_{43} of 240 minutes or greater were considered ablated tissues (Damianou C., 1994). Figure 3-2A and B are three-dimensional images of the four lesions produced at the axial and lateral limits for the smallest tumor in the peripheral zone and the largest tumor in the transitional zone respectively. The area colored in red in Figures 3-2 A and B are tissues that have a T_{43} equal to or greater than 240 minutes and the prostate is labeled in blue.
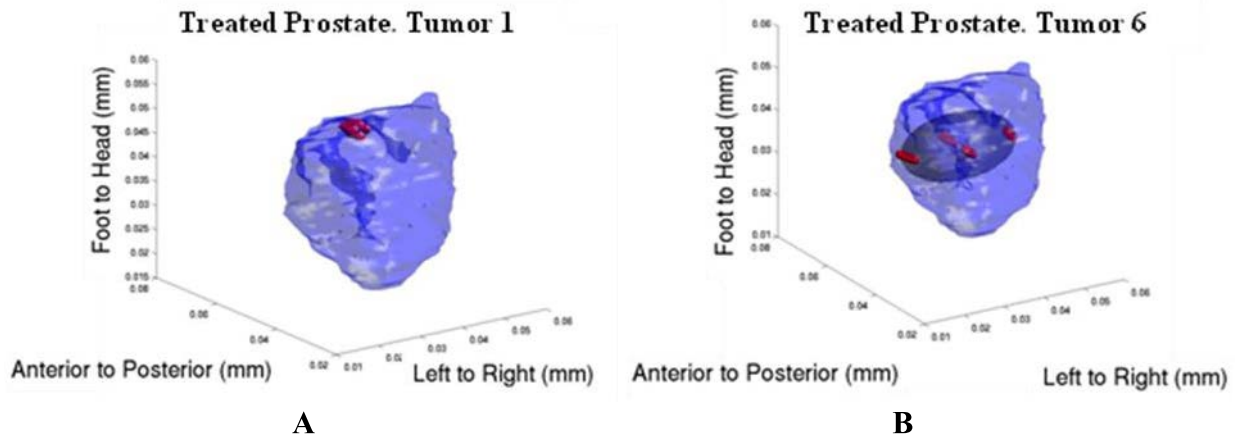
Figure 3-2. In both A and B the red ellipses are the simulated lesions and the tumors are in black. The smallest tumor in the peripheral zone (A) and the largest tumor in the transitional zone (B)

The desired lesion placement was achieved for the lateral and axial limits for all of the tumors accept tumors 2 and 3. Table 3-2 summarizes the relevant tumor information and also includes an indication of the presence of secondary lesion from the applied acoustic field. If any of the tested sites within each tumor had a secondary lesion it was considered a failed treatment simulation.

Table 3-2. Tumor Information and Secondary Lesions

Tumor Number	Tumor Size (cc)	Zonal Location	Presence of Secondary Lesions
1	0.02	Peripheral	No
2	0.79	Peripheral	Yes (Failed Treatment)
3	3.70	Peripheral	Yes (Failed Treatment)
4	0.04	Transitional	No
5	2.70	Transitional	No
6	0.80	Transitional	No

As shown in Table 3-2 tumors 2 and 3 failed the simulated treatment. In the treatment of the posterior limits for both these tumors secondary lesions were present. This is due to the nature of the normal wave propagation of sound at treatment locations close to the device. The reason for this limited focusing close to the device is that the phase differences of the elements that are at the edges of the device were extremely different to those near the center. This created a secondary lesion at depth (approximately twice the distance to the target) behind the intended lesion site. Also the lateral limits for tumor 3 fail to be treated without the production of secondary lesions. This is due to the fact that the focal region was being steered outside of its safe range.

Partial Excitation and Device Rotation

When focusing close to the device, or at the farthest lateral limits from the device center, secondary lesions were observed (see Table 3-2). Two solutions were tested to correct the production of these secondary lesions; partial excitation of the device elements and device rotation.

For the partial excitation of the device, the elements closest to the center of the device were excited on a percent basis to decrease the phase difference between elements. The maximum number of excited elements needed to be determined to minimize the acoustic intensity at the surface of the device. Determining this maximum number of elements was done by performing a number of simulations in which the number of excited elements was increased from %50 to %75 by steps of %1 until a secondary lesion was produced. Once a secondary lesion was produced the maximum number of excited elements was determined that would enable the formation of a lesion at the given location without producing secondary lesions. This simulation was performed for both posterior limits of tumors 2 and 3. Figure 3-3 shows a %56 excitation of the device elements, 431 out of the 761 elements, which is the maximum number of elements that can be used for safely treating the posterior limit of tumor 3 (located at 2.2cm from the device center). The excited elements are colored in blue and the inactive elements are colored in red. The posterior limit of tumor 2 required %71 of the transducer elements (545 out of the 761 elements) to be active in order to safely treat the location at 2.3cm from the device center.

Treating the lateral limits of tumor 3 without producing secondary lesions was done by rotating the device inside the rectum. The reason for this rotation is that these locations were out of the range of the steering capability of the device and simulations showed that without this rotation, secondary lesions were being created throughout the pelvic region. These secondary lesions were observed in a large volume approximately 1cm anterior both above and below the

intended target. The device was rotated by $\pm$ $\pi/8$ for both the left and right limits of tumor 3 respectively.
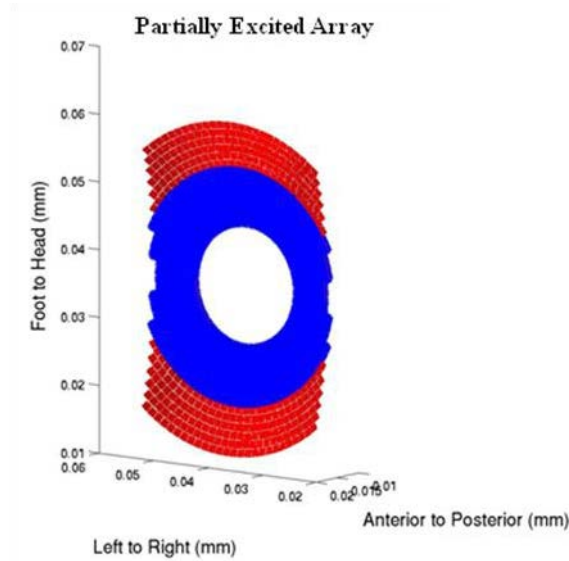
Figure 3-3. Sub Selecting elements for focusing close to the transducer. Excited elements are colored blue, and inactive elements are colored red.

Adequate focusing and lesion formation was possible for the lateral, anterior and posterior limits for all of the simulated tumors by aligning the center of the device with the tumor centers, by rotating the device, or by using the percent excitation method explained previously. The exposure time for the creation of all of these lesions was 5s. Table 3-3 summarizes some relevant information about the lesions produced in the simulation.

Table 3-3. Lesion Information

		Tumor 1	Tumor 2	Tumor 3	Tumor 4	Tumor 5	Tumor 6
Lesion Volume (cc)	Min.	0.007	0.003	0.006	0.005	0.013	0.006
	Max.	0.010	0.005	0.008	0.007	0.015	0.008
	Mean	0.009	0.004	0.007	0.006	0.014	0.007
	Std. Dev.	0.001	0.001	0.001	0.001	0.001	0.001
Acoustic Power (W)	Min.	57.35	21.09	36.46	22.87	26.70	18.91
	Max.	72.33	67.17	115.99	26.25	97.06	32.85
	Mean	66.81	42.79	71.71	24.20	60.96	24.28
	Std. Dev.	6.57	19.19	33.99	1.80	33.90	5.99
Acoustic Intensity at Transducer Surface (W/cm^2)	Min.	6.18	2.27	3.93	2.47	2.88	2.04
	Max.	7.80	10.12	22.74	2.83	10.46	3.54
	Mean	7.20	5.33	10.29	2.61	6.57	2.62
	Std. Dev.	0.71	3.38	8.50	0.19	3.65	0.645
% of active elements		%100	%71 (posterior limit)	%56 (posterior limit)	%100	%100	%100

The overall maximum acoustic intensity at the surface of the transducer for the creation of all the simulated lesions was 22.74W/cm^2. This maximum occurred when focusing at the posterior limit of tumor 3. This intensity is high as a result of the reduced surface area on the transducer when only %56 of the total available surface area is being used for the creation of the lesion.

Thermal Simulation Discussion

The thermal simulation was conducted to determine the heating effects of the device on the tissue in the male pelvis region. As outlined previously the capabilities of the device to produce a thermal lesions at the lateral, posterior and anterior limits of each simulated tumor were tested. The reason for selecting only these limits was to demonstrate the ability to focus throughout the tumor without having to simulate lesions over the entire simulated mass.

The device was able to treat all but four locations at the limits of all the simulated tumors. The problems occurred for the locations closest to the device center in the axial direction and farthest from the device center in the lateral direction. The two locations closest to the device center in the axial direction were situated at 2.2 and 2.3cm from the center of the device. To solve this problem a partial excitation of the device elements was proposed. An algorithm for determining the optimal number of excited elements for treatment locations that are close to the device center needs to be developed for proper treatment of these zones. The other two locations that were problematic to create lesions at were the lateral limits of the largest tumor (tumor 3). Rotating the device allowed producing lesions at these locations without secondary effects.

In this study the device was aligned with the center of each tumor so that the effects of steering the acoustic field could be tested. It was apparent in the treatment of the lateral limits of tumor 3 that some device rotation is required for creating lesions in targeted areas far from the center of the device in the lateral direction. In a practical setting it would be well advised to rotate the device so that the center of the device in the lateral direction is approximately aligned with the desired location of the lesion. This would provide a better focus and better lesion placement.

The maximum, minimum and standard deviation of the lesion volumes observed was 0.015 cc, 0.003cc and 0.003 respectively. This range in lesion volume is due to the distance of the desired lesion location from the center of the device in the axial direction. Lesions produced at a greater distance are long in the axial direction. This effect is in direct relationship to the elliptical focus of the device that was discussed in the acoustic simulation discussion. Another algorithm needs to be developed to estimate lesion size based on the target distance from the transducer center as it is apparent there is a large difference in their volumes.

Section 5: Discussion and Conclusions

The purpose of this study was to determine the feasibility of designing a new dual-modality trans-rectal HIFU device for localized prostate cancer treatment. Development of the environment for this study was done suing images from the VHSMP. These images were used to reconstruct the organs in the male pelvis region. Also simulated tumors were placed within the reconstructed prostate to adequately test the treatment capabilities of the device.

The three tested device configurations were the concentric ring array, the randomly placed circular elements array and the randomly excited concentric ring array. Out of the three tested devices the concentric ring array device was the optimal configuration for treatment of the prostate gland. The parameters that were varied for the parametric study of the concentric ring array were the focal length, the operating frequency, the element size and the central opening radius to lodge the imaging transducer. Determining the optimal combination of these parameters was done by simulating the acoustic field and calculating the ratio of the primary and the secondary lobes (η) of the acoustic field. The simulated device with the minimal amount of independent elements which had $\eta \leq 0.5$ was selected as the optimal device. The optimal device parameters that were found were a focal length of 68mm, an operating frequency of 2.75MHz, an elements size of 2.05λ and a central opening radius for lodging the imaging transducer of 9mm. The total number of independent elements for this configuration was 761.

The random circular array was tested to observe if random elements could reduce secondary lobes. Due to the lack of therapeutic treatment surface area the device was not able to focus at the chosen test locations and the steering capability of this device was also limited due to the lack of symmetry of the therapeutic elements.

The randomly excited array was also simulated to determine if random excitation could reduce the secondary lobes of the acoustic field. Again, just as the random circular array simulation, the lack of therapeutic surface area inhibited the device from focusing at all the test locations. Since focusing on the transducer center axis was not possible there was no need to test the steering capability of this randomly excited device.

Finally a simulation of the thermal effects was conducted by implementing the Bio-Heat Transfer Equation to obtain the temperature rise produced by the device at different treatment locations. Test locations were defined in order to treat the lateral, anterior and posterior limits of different simulated tumors. When testing the different treatment locations the device was aligned to the center of the tumors. However, for the largest tumor a rotation of $\pm \pi/8$ was required to treat both lateral limits respectively. This was required because those test locations were out of the steering capabilities of the device. In future applications the device should be aligned as close as possible to the treatment location and the electronic dynamic focusing should be used to further increase the focus of the device at the proper target site.

For two of the simulated tumors the treatment of the posterior limits was not possible since secondary lesions appeared. These locations were at 2.2 and 2.3cm from the center of the device. For treating these locations the device elements were partially activated. Practically this device should be aligned with the desired treatment location and then the electronic dynamic focusing should be used to further focus the acoustic energy at the desired target. The maximum

steering required for a specific lesion size needs to be determined and a safety limit needs to be determined to optimize the treatment. Mechanical rotation should be limited but it most likely will be required for treating large tumor masses or prostates with multiple tumors. This requirement of rotation to cover this type of tumor mass is not necessary a problem. A rotation mechanism is still required to position the device at the center of a tumor mass. For this type of enlarged tumor, the treatment can be divided in sub-regions and the electronic steering will be able to cover the sub-regions.

It is apparent that the simulated concentric ring array has the ability to create small lesions within the prostate. Further work is required to determine the optimal treatment regime required for treating entire tumor masses within the prostate. Parameters that need to be examined would include exposure time, surface intensity and maximum reached temperatures. In the current study the heat accumulation after successive exposures was not examined. The heat accumulation needs to be examined as it may have an effect on the treatment regime.

Another consideration for the future simulation would be the locations at which partial percent excitation is required for adequate treatment. In the simulation presented in this paper it was found that treatment locations that are less than 2.3cm from the center of the device require a partial excitation of the independent elements on the device. However, we only tested some points; a more general study has to be conducted. As well, the optimal percentage of independently excited elements that is required for treatment at other locations has to be confirmed.

After deciding upon a treatment regime based on the results of a treatment regime study, the next step in the development of this device would be construction and physical testing. Although the optimal element size is 2.05λ with a minimum element spacing of $\lambda/4$ the construction of the therapeutic portion of this device may not be possible due to constraints on the material fabrication. The constructed device may have slightly larger therapeutic elements, or a slightly larger spacing between elements. The impact of these variations should be studied as well.

In this study we examined an optimal device that would need an ultrasound imaging probe smaller than the one currently used by the Ablatherm[TM] system. The existing probe is a linear array operating at 8MHz. The diameter of the central opening used to lodge the imaging probe went from 25mm to 18mm. A study can be performed to design a new imaging probe that can be compatible with this central opening. The size of this central opening is at least compatible with existing probes used in trans-esophageal imaging systems for cardiac imaging (Bezold L.I., 1996) which shows dimensions in the order of 13 mm, including protective case. On the other hand, the operating frequency of these probes is in the range between 3 and 5MHz. The new study can analyze the maximal frequency that can be attained with the new dimension of the central opening.

Another possible solution is to fill the central opening with dual operational transducers that can image the prostate and treat the prostate. The elements of the device that are located near the center of the treatment area could be dual imaging and therapy transducer elements (Owen N.R., 2010). A combination of imaging elements and imaging/therapy elements could be constructed in this space and used when necessary, such as for treating distant targets.

There exists also the possibility of keeping the best device found with the central opening large enough the existing imaging probe. This device seems able to treat precise regions up to a region found at a depth of 50-mm (Figure 2-14). Deeper regions may be attained with longer exposures; the limitation of this approach may be that the selectivity of treating small regions

will be reduced. However, the anterior region of the prostate is surrounded by fat tissue and there are not delicate structures to preserve in this region.

Another matter that has to be studied concerns the MR imaging. An MRI coil will have to be embedded within the device and this will certainly modify the geometrical characteristics and possibly impact the ergonomics of the device. The device proposed in this study is intended to use MRI for real time feed-back of temperature changes within the prostate and surrounding tissue. A complete study of the geometry and placement of the MRI coil, within the device, needs to be conducted to optimize the MRI imaging and to evaluate its impact on the performance of the device.

The computation time for calculating the acoustic field using the GPU's was approximately %60 shorter that of the cluster computer system. Having much shorter computation times meant that this parametric study, and any after it, could be run for larger variations of parameters. This gives the user of the simulation more freedom to perhaps include more variables in the simulation or to simulate more configurations in the same amount of time. Also the cost of the GPU system is considerably less than that of the cluster computer. This could relate to more investigators having the opportunity to simulate their ideas at an affordable expense and hence lessen their time in physical experimentation. The advent of using GPU's for computer simulation is decreasing costs and increasing simulations times in many other engineering simulation applications (Walsh S.D.C., 2009) and the medical research community will benefit from these advances as well.

Appendix

Numerical Implementation
Graphics Processing Unit and CUDA

NVIDIA Tesla 1060 graphics processors were used in this study for calculating the acoustic field and thermal effects from HIFU treatment. The reason for using these processors is that they are less expensive, to purchase and to house, and are suitable for high arithmetic applications (Owens, J., 2008). GPU's are suitable for high arithmetic applications because, unlike central processing units, they pipeline tasks in space not time. Also the amount of transistors dedicated to data processing in GPU's is higher as the GPU requires less data caching and flow control then central processing units (CPU). The main disadvantage of a GPU is that it is not suitable for all computing applications, such as an operating system or network connection, as it is only capable of supporting mathematical and memory access instructions. There are two major components that execute code when using a GPU; the host, a CPU, and the device, the GPU. The host passes the necessary information for calculation to the device which is saved into memory.

Computer Unified Device Architecture (CUDA) is a general purpose parallel computing architecture developed by NVIDIA to program their GPU's in a variety of computer languages (Kirk, D.B, 2009). In a GPU each task is executed by a thread. All of the threads in a GPU are grouped together in blocks and can be indexed either one dimensionally or two dimensionally. The host will call functions named *kernels* that will be executed by the GPU using a grid block distribution of threads.

The architecture of the modern GPU consists of threads, local memory, shared memory, global memory, constant memory, texture memory and registers (see Figure A-1). The efficient use of these resources is at the discretion of the programmer. The local memory is the memory associated to each thread inside of a block. This memory is only accessible by the thread it pertains to and not directly accessible to other threads within the same block. Shared memory is available to all of the threads within the particular block it pertains to. It is not directly accessible to other blocks. Global memory is available to all of the blocks within the GPU but it is a costly memory access and should be avoided for minimizing simulation time. Texture memory is also available to all of the blocks within the GPU. CUDA supports a subset of the texturing hardware which uses this memory which is not pertinent to this particular simulation environment. The registers in the GPU are another writing resource for individual threads.
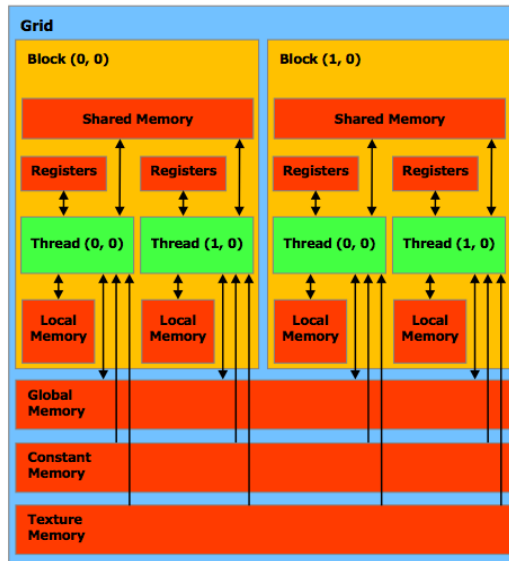
Figure A-1. Architecture of GPU

Threads are indexed based on a block index and a thread index (see Figure A-2).
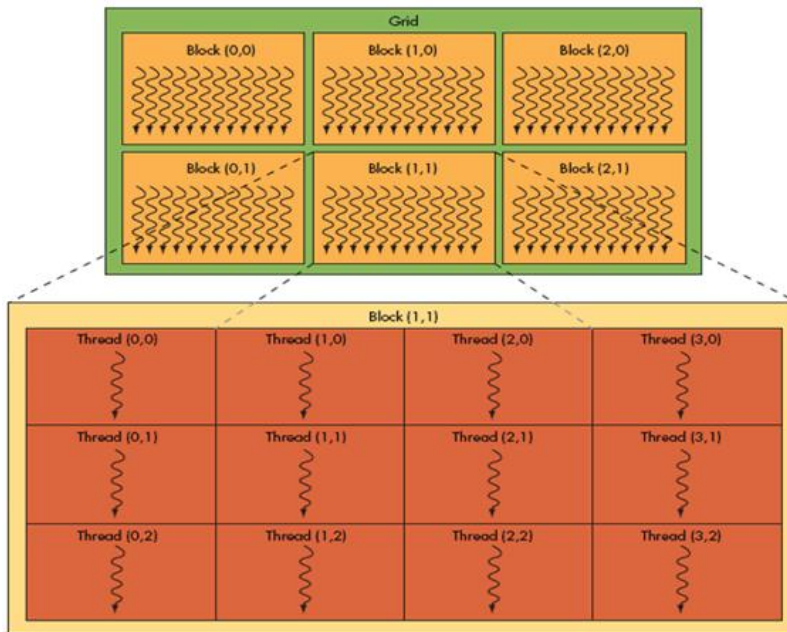

Figure A-2. Block and thread indexing for GPU.

The number of threads required to execute the *kernel* for one block of threads is the thread block dimension and the number of block grids required to execute the entire parallelized instruction is the block grid dimension.

Acoustic Field Calculation Algorithm

The acoustic field simulation was programmed in Matlab with a mexFunction used to execute the GPU code. The numerical version of (2.1) that was coded is

$$\varphi(r) = \frac{1}{2\pi}\sum_{\psi=1}^{N} v_{s_\psi} \frac{e^{ikR_\psi - \alpha_\psi}}{R_\psi} ds_\psi \qquad (\text{A-1})$$

Using a back propagation scheme the Matlab function first calculated the phase and amplitude of each sub-element ψ, in the virtually constructed array, required to create a focal region at the desired location. Then an observation field of data points was constructed in a Cartesian three-dimensional domain at a resolution of $\lambda/2$. This domain of data was sent to the global memory of the GPU.

The mexFunction dedicated the amount of constant memory available for each block of the *kernel* computation. The data sent to the constant memory in the GPU included the phase and amplitude of the signal, location and surface area for each sub-element ψ, the acoustic attenuation of the media in the study and the speed of sound. The constant memory allocation is calculated by dividing the total constant memory, 64kB, by the amount of memory required to allocated the data describing a sub-element ψ. For this calculation, the maximum number of sub-elements ψ that could be fitted was 2700. This implies that the *kernel* needs to be called enough times to calculate the full integral, where each time 2700 sub-elements are sent to the constant memory. The optimal thread block dimension was determined experimentally by running the simulation with different block sizes until the optimized size was determined, which was a one-dimensional block of 256 threads. The grid dimension was calculated as follows:

Block grid dimension = (number of sources – 1/thread block dimension + 1)   (A-2)

Calculating the acoustic field at each observation point was done by summing the acoustic field from each source produced by each sub-element ψ in the array. As mentioned above, the *kernel* was called enough times to calculate the full contribution of the device. The call to the *kernel* was as follows:

```
while(mr1start < mr1)
  {
   mr1stop = mr1start+MAX_ELEMS_IN_CONSTANT;
   if (mr1stop >= mr1)// if the last block of data has been accessed then this is the last time the loop will run
    {
     mr1stop =  mr1;
     LastPart=1;
    }
```

ForwardPropagationKernel<<<dimBlockGrid, dimThreadBlock>>>(mr2,

    mr1,
    wvnbr,
    wvnbi,
    d_r2pr,
    d_u2pr,
    d_u2pi,
    mr1step,
    LastPart,
    d_coolant_ellipse,
    d_distended_ellipse,
    prostate_attenuation);

CHECK_LAST_ERR();// error check to ensure all calculations were done
cudaThreadSynchronize();// this command makes sure the program waits for all the threads to be done calculating
before continuing with the execution.

    The *kernel* function used for calculating the acoustic is given below under the header
__global__ void ForwardPropagationKernel:

```
__global__ void ForwardPropagationKernel(const unsigned int mr2,
            const unsigned int mr1,
            const cudaFloatingType wvnbr,
            const cudaFloatingType wvnbi,
            cudaFloatingType *r2pr,
            cudaFloatingType *u2pr,
            cudaFloatingType *u2pi,
            const unsigned int mr1step,
            const char LastPart,
            cudaFloatingType *coolant_ellipse,
            cudaFloatingType *distended_ellipse,
            cudaFloatingType prostate_attenuation)
```

```
const int si2 = blockDim.x * blockIdx.x + threadIdx.x ;//setting indexing for threads as a 1D grid
if ( si2 >= mr2) // each data point is saved in mr2 and is indexed by si2
  return;
  temp_r = 0;
  temp_i = 0;
  for (int si1=0; si1<mr1step; si1++) // each source is saved in mr1 and is indexed by si1
   {dx=PartSource[si1]-r2pr[si2];
    dy=PartSource[si1+mr1step]-r2pr[si2+mr2];
    dz=PartSource[si1+2*mr1step]-r2pr[si2+2*mr2];
    R=sqrt(dx*dx+dy*dy+dz*dz);// distance between source and data point
    //get normal vector
    dx=abs(dx/R);
    dy=abs(dy/R);
    dz=abs(dz/R);
    //initialize intersection distance to zero, if we cross the ellipses then we will change them
```

```
      R2=0;
      R3=0;
      R1=sqrt(intrp[0]*intrp[0]+intrp[1]*intrp[1]+intrp[2]*intrp[2]);// inside coolant ellipse
      if (R1>=R){//inside coolant ellipse
       R1=R;
      }
      else { //point is between coolant ellipse and distended ellipse
        ellipse_intersection(CONST_distended_ellipse,dx,dy,dz,PartSource,si1,mr1step,intrp);//calculating
ellipse intersection for both coolant ellipse and distended rectum ellipse
       R2 = sqrt(intrp[0]*intrp[0]+intrp[1]*intrp[1]+intrp[2]*intrp[2]);
       if (R2>=R){//inside distended ellipse
        R2=R-R1;
       }
       else {//point is outside all ellipses
        R2-=R1;
        R3=R-R2-R1
      atten_fact=-(CONST_coolant_ellipse[5]*R1 + CONST_distended_ellipse[5]*R2 +
      CONST_prostate_attenuation*R3);
      atten_fact=__expf(atten_fact);//*R);
      ti=atten_fact*Part_a1pr[si1]/R;
      tr=ti;
      __sincosf(R*wvnbr,&pSin,&pCos);
      tr*=(Part_u1pr[si1]*pCos-Part_u1pi[si1]*pSin);
      ti*=(Part_u1pi[si1]*pCos+Part_u1pr[si1]*pSin);
      temp_r +=tr;
      temp_i +=ti;
    }//End of for si1
   u2pr[si2]+=temp_r;
   u2pi[si2]+=temp_i;
}
```

BHTE Calculation algorithm

The thermal simulation was programmed as a Matlab function with a mexFunction used to execute the GPU code. The acoustic field required for treatment of the selected target site was determined using the technique previously explained. Using the masks created from the VHSMP, matrices were created to represent the tissue perfusion rate, thermal conductivity, specific heat, acoustic absorption and, for the coolant liquid, a flow rate matrix. These matrices were passed into global memory. Constant memory was used to store the exposure time, blood properties, initial temperature settings and the observation field creating an array of tissue information. The BHTE was then run in succession until a steady temperature state was reached (see section 3) with the Finite Difference Time Difference technique defined by Yin *et al.* (2006). The implementation of the Finite Difference Time Difference technique will now be explained.

The computation of the BHTE was modeled in Cartesian space and the discretized using equation A-2.

$$T_{i,j,k}^{n+1} = T_{i,j,k}^n + \frac{\Delta t}{\rho_{t_{i,j,k}} c_{t_{i,j,k}}} \times \left\{ \begin{array}{c} K_{t_{i,j,k}} \left[\mathbf{P}\left(T_{i,j,k}^n, x_i\right) + \mathbf{Q}\left(T_{i,j,k}^n, y_i\right) + \mathbf{R}\left(T_{i,j,k}^n, z_i\right) \right] \\[2mm] -\omega_{i,j,k} C_{b_{i,j,k}} \left[T_{i,j,k}^n - T_\alpha \right] + \frac{x_{i,j,k} |p_{i,j,k}|^2}{\rho_{t_{i,j,k}} c_{b_{i,j,k}}} \end{array} \right\} \qquad \text{(A-3)}$$

where:
$$\mathbf{P}\left(T_{i,j,k}^n, x_i\right) = \frac{\left(\frac{T_{i-1,j,k}^n - T_{i,j,k}^n}{x_{i-1}^n - x_i^n} - \frac{T_{i,j,k}^n - T_{i+1,j,k}^n}{x_i^n - x_{i+1}^n} \right)}{\left(\frac{x_{i-1}^n + x_i^n}{2} - \frac{x_i^n + x_{i+1}^n}{2} \right)}$$

$$\mathbf{Q}\left(T_{i,j,k}^n, y_j\right) = \frac{\left(\frac{T_{i,j-1,k}^n - T_{i,j,k}^n}{y_{j-1}^n - y_j^n} - \frac{T_{i,j,k}^n - T_{i,j+1,k}^n}{y_j^n - y_{j+1}^n} \right)}{\left(\frac{y_{j-1}^n - y_j^n}{2} - \frac{y_j^n + y_{j+1}^n}{2} \right)}$$

$$\mathbf{R}\left(T_{i,j,k}^n, z_k\right) = \frac{\left(\frac{T_{i,j,k-1}^n - T_{i,j,k}^n}{z_{k-1}^n - z_k^n} - \frac{T_{i,j,k}^n - T_{i,j,k+1}^n}{z_k^n - z_{k+1}^n} \right)}{\left(\frac{z_{k-1}^n - z_k^n}{2} - \frac{z_k^n + z_{k+1}^n}{2} \right)}$$

Each element in the tissue array was assigned to a thread. As seen in equation A-3 each element in the array of data points is dependent on the elements in front and behind it. Therefore elements at the edge of each block will have a dependency on the block previous to it.

To speed-up calculations, shared memory was used to store temporarily thermal properties of threads that were neighbors in the same thread block. As stated earlier each block of threads can only access the shared memory of that particular block and accessing global memory incorporates latency in memory access. Therefore to ensure that the boundaries of each block are properly calculated a padding technique in which an overlap of calculations was implemented. The thread indexing had to be changed from that seen in equation A-1 to the following:

$$i = (Blockindex.x)\big(BlockDim.x - (Padding \times 2)\big) + ThreadIndex.x - Padding \quad \text{(A-4)}$$
$$j = (Blockindex.y)\big(BlockDim.y - (Padding \times 2)\big) + ThreadIndex.y - Padding \quad \text{(A-5)}$$
$$k = ThreadIndex.z - Padding \qquad \text{(A-6)}$$

It can be seen in equations A-4 and A-5 that the indexing was reduced by doubling the padding to correct for both sides of the padding and then shifted for proper indexing on both sides of the tissue array. The indexing for the third dimension, equation A-6, is not indexed since the thread hierarchy is two dimensional. The third dimension was spliced and the index was iterated internally with a *for* loop.

Now that the steady state conditions were determined the BHTE mexFunction was run again to determine the power ratio required for delivering the desired thermal dose. The acoustic absorption matrix was then multiplied by this ratio and the BHTE was run a final time to produce the desired thermal does and the lesion prediction was complete and displayed in a three dimensional image with examples seen in Figure 3-2.

References

Arterbery, E.V., MD., Frazier, A., MD., Dalmia, P., MS., Siefer, J., DO., Lutz, M., MD. & Porter, A., MD. 1997, "Quality of Life After Permanent Prostate Implant", Seminars in Surgical Oncology, vol. 13, no. 6, pp. 461-464.

Bamber, J.C. & Hill, C.R. 1979, "Ultrasonic attenuation and propagation speed in mammalian tissues as a function of temperature", Ultrasound in medicine & biology, vol. 5, no. 2, pp. 149-157.

Bezold, L.I., MD., Pignatelli, R., MD., Altman, A.C., MD., Feltes, T.F., MD., Gajarski, R.J., MD., Vick, G.V.3rd., MD., PhD., & Ayres, N.A., MD. 1996, "Intraoperative transesophageal echocardiography in congenital heart surgery. The Texas Children's Hospital experience.", Tex Heart Inst J., vol. 23, no. 2, pp. 108-115.

Black M. J., Hawks H. J. 2009, Medical-Surgical Nursing, 8th edn, Elsevier.

Blana, A., Murat, F.J., Walter, B., Thuroff, S., Wieland, W.F., Chaussy, C. & Gelet, A. 2008, "First Analysis of the Long-Term Results with Trans-rectal HIFU in Patients with Localised Prostate Cancer", European urology, vol. 53, no. 6, pp. 1194-1203.

Chapelon, J.Y., Faure, P., Plantier, M., Cathignol, D., Souchon, R., Gorry, F. & Gelet, A. 1993, "The Feasibility of Tissue Ablation using High Intensity Electronically Focused Ultrasound.", Ultrasonics Symposium, IEEE 1993, pp. 1211.

Chapman, A. & ter Haar, G. 2007, "Thermal ablation of uterine fibroids using MR-guided focused ultrasound-a truly non-invasive treatment modality", European radiology, vol. 17, no. 10, pp. 2505-2511.

Chavrier, F., Chapelon, J.Y., Gelet, A. & Cathignol, D. 2000, "Modeling of high-intensity focused ultrasound-induced lesions in the presence of cavitation bubbles", The Journal of the Acoustical Society of America, vol. 108, no. 1, pp. 432-440.

Chin, J.L., Downey, D.B., Mulligan, M. & Fenster, A. 1998, "Three-Dimensional Transrectal Ultrasound Guided Cryoablation for Localized Prostate Cancer in Nonsurgical Candidates: A Feasibility Study and Report or Early Results", The Journal of urology, vol. 159, no. 3, pp. 910-914.

Chen, Q., Huang, Z., Luck, D., Beckers, J., Brun, P., Wilson, B.C., Scherz, A., Salomon, Y. & Hetzel, F.W. 2002, "Preclinical Studies in Normal Canine Prostate of a Novel Palladium-Bacteriopheophorbide (WST09) Photosensitizer for Photodynamic Therapy of Prostate Cancer", Photochemistry and Photobiology, vol. 76, no. 4, pp. 438-445.

Chodak, G.W., Thisted, R.A., Gerber, G.S., Johansson, J., Adolfsson, J., Jones, G.W., Chisholm, G.D., Moskovitz, B., Livne, P.M. & Warner, J. 1994, "Results of Conservative Management of Clinically Localized Prostate Cancer", N Engl J Med, , no. 330, pp. 242-248.

Chopra, R., Tang, K., Burtnyk, M., Boyes, A., Sugar, L., Appu, S., Klotz, L. & Bronskill, M. 2009, "Analysis of the spatial and temporal accuracy of heating in the prostate gland using transurethral ultrasound therapy and active MR temperature feedback", Physics in Medicine and Biology, vol. 54, no. 9, pp. 2615-2633.

Coakley, F.V., MD, Kurhanewicz, J., PhD, Lu, Y., PhD, Jones, K.D., MD, Swanson, M.G., PhD, Chang, S.D., MD, Carroll, P.R., MD & Hricak, H., MD PhD 2002, "Prostate Cancer Tumor Volume: Measurement with Endorectal MR and MR Spectroscopic Imaging", Radiology, vol. 223, no. 1, pp. 91-97.

Cobbold, R.S.C. 2007, Foundations of Biomedical Ultrasound, 1st edn, Oxford University Press, New York.

Colombel, M. & Gelet, A. 2004, "Principles and results of high-intensity focused ultrasound for localized prostate cancer.", Prostate Cancer and Prostatic Deseases, vol. 7, no. 4, pp. 289-294

Crouzet, S., Rebillard, X., Chevallier, D., Rischmann, P., Pasticier, G., Garcia, G., Rouviere, O., Chapelon, J. & Gelet, A. 2010, "Multicenter Oncologic Outcomes of High-Intensity Focused Ultrasound for Localized Prostate Cancer in 803 Patients", Eur. Urol, vol. 58, no. 4, pp. 39.

Curiel, L. 2001, Application de la Focalisation Dynamique a la Chirurgie Ultrasonore. Etude de deux configuration: Reseau Annulaire et Barrette 1.5D, L'Institut National des Science Appliques de Lyon.

Curiel, L., Chopra, R. & Hynynen, K. 2009, "In Vivo Monitoring of Focused Ultrasound Surgery Using Local Harmonic Motion", Ultrasound in medicine & biology, vol. 35, no. 1, pp. 65-78.

Curiel, L., Chopra, R. & Hynynen, K. 2009, "In Vivo Monitoring of Focused Ultrasound Surgery Using Local Harmonic Motion", Ultrasound in medicine & biology, vol. 35, no. 1, pp. 65-78.

Damianou, C.A., Hynynen, K. & Fan, X. 1995, "Evaluation of accuracy of a theoretical model for predicting the necrosed tissue volume during focused ultrasound surgery", Ultrasonics, Ferroelectrics and Frequency Control, IEEE Transactions on, vol. 42, no. 2, pp. 182-187.

Damianou, C. & Hynynen, K. 1994, "The effect of various physical parameters on the size and shape of necrosed tissue volume during ultrasound surgery", The Journal of the Acoustical Society of America, vol. 95, no. 3, pp. 1641-1649.

D'Amico, A.V., Tempany, C.M., Cormack, R., Hata, N., Jinzaki, M., Tuncali, K., Weinstein, M. & Richie, J.P. 2000, "Transperineal Magnetic Resonance Image Guided Prostate Biopsy", The Journal of urology, vol. 164, no. 2, pp. 385-387.

De Angelis, G., Rittenhouse, H.G., Mikolajczyk, S.D., Blair Shamel, L. & Semjonow, A. 2007, "Twenty Years of PSA: From Prostate Antigen to Tumor Marker", Reviews in urology, vol. 9, no. 3, pp. 113-123.

Diederich, C.J., Nau, W.H., Burdette, E.C., Khalil Bustany, I.S., Deardorff, D.L. & Stauffer, P.R. 2000, "Combination of transurethral and interstitial ultrasound applicators for high-temperature prostate thermal therapy", International Journal of Hyperthermia, vol. 16, no. 5, pp. 385-403.

Diederich, C.J. & Burdette, E.C. 1996, "Transurethral ultrasound array for prostate thermal therapy: initial studies", Ultrasonics, Ferroelectrics and Frequency Control, IEEE Transactions on, vol. 43, no. 6, pp. 1011-1022.

Diederich, C.J. & Hynynen, K. 1991, "The feasibility of using electrically focused ultrasound arrays to induce deep hyperthermia via body cavities", Ultrasonics, Ferroelectrics and Frequency Control, IEEE Transactions on, vol. 38, no. 3, pp. 207-219.

Duck, F.A. 1990, Physical properties of tissue: a comprehensive reference book, Academic Press, London, UK.

Eastham, J.A., Kattan, M.W., Rogers, E., Goad, J.R., Ohori, M., Boone, T.B. & Scardino, P.T. 1996, "Risk Factors for Urinary Incontinence after Radical Prostatectomy", The Journal of urology, vol. 156, no. 5, pp. 1707-1713.

Ecole Polytechnique Federal de Lausanne, Computer Science Dept. 1998, Visible Human Server [2009, 10/8] .

EDAP TMS 2010, 12/31-last update, Ablatherm HIFU [2010, 7/15].

Fan, X. & Hynynen, K. 1992, "The effect of wave reflection and refraction at soft tissue interfaces during ultrasound hyperthermia treatments", J. Acoust. Soc. Am., vol. 91, no. 3, pp. 1727-1736.

Flynn, H.G. 1982, "Generation of transient cavities in liquids by microsecond pulses of ultrasound", J. Acoust. Soc. Am., vol. 72, no. 6, pp. 1926-1932.

FreedBerg, I.M., MD., Eisen, A.Z., MD., Wolff K., D., Austen, F.K., MD., Goldsmith, L.A., MD., Katz, S. I., MD PhD. & Fitzpatrick, T. B., MD PhD DSc. 1999, "Thermoregulation" in Fitzpatrick's Dermatalogy in General Medicine, 5th edn, McGraw Hill, United States, pp. 175.

Gelet, A., Chapelon, J.Y., Bouvier, R., Pangaud, C. & Lasne, Y. 1999, "Local Control of Prostate Cancer by Trans-rectal High Intensity Focused Ultrasound Therapy: Preliminary Results", The Journal of urology, vol. 161, no. 1, pp. 156-162.

Hamilton, A.S., Stanford, J.L., Gilliland, F.D., Albertsen, P.C., Stephenson, R.A., Hoffman, R.M., Eley, J.W., Harlan, L.C. & Potosky, A.L. 2001, "Health Outcomes After External-Beam Radiation Therapy for Clinically Localized Prostate Cancer: Results From the Prostate Cancer Outcomes Study", Am. Soc. Clin. Onc., vol. 19, no. 9, pp. 2517-2526.

Han, K.R., Cohen, J.K., Miller, R.J., Pantuck, A.J., Freitas, D.G., Cuevas, C.A., Kim, H.L., Lugg, J., Childs, S.J., Shuman, B., Jayson, M.A., Shore, N.D., Moore, Y., Zisman, A., Lee, J.Y., Ugarte, R., Mynderse, L.A., Wilson, T.M., Sweat, S.D., Zincke, H. & Belledegrun, A.S. 2003, "Treatment of Organ Confined Prostate Cancer with Third Generation Cryosurgery: Preliminary Multicenter Experience", The Journal of urology, vol. 170, no. 4, pp. 1126-1130.

Hazle, J.D., Diederich, C.J., Kangasniemi, M., Price, R.E., Olsson, L.E. & Stafford, R.J. 2002, "MRI-guided thermal therapy of transplanted tumors in the canine prostate using a directional transurethral ultrasound applicator", Journal of Magnetic Resonance Imaging, vol. 15, no. 4, pp. 409-417.

Hill C.R., Bamber J.C. & ter Haar G.R. 2004, "Physical Principles of Medical Ultrasound" in , 2nd edn, John Wiley and Sons, Ltd., West Sussex, England, pp. 422-442-144-145.

Huang, Z., Chen, Q., Luck, D., Beckers, J., Wilson, B.C., Trncic, N., LaRue, S.M., Blanc, D. & Hetzel, F.W. 2005, "Studies of a vascular-acting photosensitizer, Pd-bacteriopheophorbide (Tookad), in normal canine prostate and spontaneous canine prostate cancer", Lasers in surgery and medicine, vol. 36, no. 5, pp. 390-397.

Hynynen, K. 2010, "MRI-guided focused ultrasound treatments", Ultrasonics, vol. 50, no. 2, pp. 221-229.

Illing, R. & Emberton, M. 2006, "Sonablate®-500: trans-rectal high-intensity focused ultrasound for the treatment of prostate cancer", Expert Rev. Med. Devices, vol. 6, no. 3, pp. 717-729. Kennedy, J.E. 2005, "High-intensity focused ultrasound in the treatment of solid tumours", Nature Reviews Cancer, vol.5, no. 4, pp.321.

Kirby, R.S., Partin, A.W., Feneley, M.R. & Parsons, J.K. 2000, Prostate Cancer: Principles and Practice, Taylor and Francis.

Kirk, D.B. & Hwu, W.W. 2009, Programming Massively Parallel Processors: A Hands on Approach, Morgan Kaufmann Publishers, Burlington MA, USA.

Koudinova, N.V., Pinthus, J.H., Brandis, A., Brenner, O., Bendel, P., Ramon, J., Eshhar, Z., Scherz, A. & Salomon, Y. 2003, "Photodynamic therapy with Pd-bacteriopheophorbide (TOOKAD): Successful in vivo treatment of human prostatic small cell carcinoma xenografts", International Journal of Cancer, vol. 104, no. 6, pp. 782-789.

Leighton T.G 1994, The Acoustic Bubble, Academic Press.

Lele, P.P. 1967, "Production of deep focal lesions by focused ultrasound-current status", Ultrasonics, vol. 5, no. 2, pp. 105-112.

Martini, F.H., Timmons, M.J. & Tallitsch, R.B. 2005, Human Anatomy, 5th edn, Benjamin Cummings.

Melchior, S.W. & Brawer, M.K. 1996, "Role of trans-rectal ultrasound and prostate biopsy", Journal of Clinical Ultrasound, vol. 24, no. 8, pp. 463-471.

Netsch, C., Bach, T., Gross, E. & Gross, A.J. 2011, "Rectourethral Fistula After High-Intensity Focused Ultrasound Therapy for Prostate Cancer and its Surgical Management", Urology, vol. Article in Press.

Owen, N.R., Chapelon, J.Y., Bouchoux, G., Berriet, R., Fleury, G. & Lafon, C. 2010, "Dual-mode transducers for ultrasound imaging and thermal therapy", Ultrasonics, vol. 50, no. 2, pp. 216-220.

Owens, J., Houston, M., Luebke, D., Green, S., Stone, J. & Phillips, J. 2008, "Graphics Processing Units--powerful, programmable, and highly parallel--are increasingly targeting general-purpose computing applications.", Proceedings of the IEEE. 3D Media and Displays, vol. 96, no. 5, pp. 879-899.

Pennes, H.H. 1948, "Analysis of tissue and arterial blood temperatures in the resting human forearm", J. Appl. Physiol., vol. 1, no. 2, pp. 93-122.

Petrusca L.M. 2009, Validation d'une nouvelle génération de sondes HIFU en utilisant la thermométrie IRM.

Pichardo, S., Gelet, A., Curiel, L., Chesnais, S. & Chapelon, J.Y. 2008, "New Integrated Imaging High Intensity Focused Ultrasound Probe for Trans-rectal Prostate Cancer Treatment", Ultrasound in medicine & biology, vol. 34, no. 7, pp. 1105-1116.

Pichardo, S. & Hynynen, K. 2009, "New design for an endoesophageal sector- based array for the treatment of atrial fibrillation: a parametric simulation study", IEEE Transactions on Ultrasonics, Ferroelectrics and Frequency Control, vol. 56, no. 3, pp. 600-612.

Pichardo, S. & Hynynen, K. 2007, "Circumferential lesion formation around the pulmonary veins in the left atrium with focused ultrasound using a 2D-array endoesophageal device: a numerical study", Physics in Medicine and Biology, vol. 52, no. 16, pp. 4923-4942.

Poissonnier, L., Chapelon, J.Y., Rouviere, O., Curiel, L., Bouvier, R., Martin, X., Dubernard, J.M. & Gelet, A. 2007, "Control of Prostate Cancer by Trans-rectal HIFU in 227 Patients", European urology, vol. 51, no. 2, pp. 381-387.

Poorter, J.D., Wagter, C.D., Deene, Y.D., Thomsen, C., Ståhlberg, F. & Achten, E. 1995, "Noninvasive MRI Thermometry with the Proton Resonance Frequency (PRF) Method: In Vivo Results in Human Muscle", Magnetic Resonance in Medicine, vol. 33, no. 1, pp. 74-81.

Prostate Cancer Canada Network 2009, Chemotherapy [2009, December].

Prostate Cancer Canada Network , Surgery [2009, November].

Public Health Agency of Canada 2009, Special Topic: Cancer in Adolescents and Young Adults, Canadian Cancer Society, Statistics Canada, Provincial/Territorial cancer Registries [2009, November].

Raz, O., Haider, M.A., Davidson, S.R.H., Lindner, U., Hlasny, E., Weersink, R., Gertner, M.R., Kucharcyzk, W., McCluskey, S.A. & Trachtenberg, J. 2010, "Real-Time Magnetic Resonance Imaging–Guided Focal Laser Therapy in Patients with Low-Risk Prostate Cancer", European urology, vol. 58, no. 1, pp. 173-177.

Ross, A.B., Diederich, C.J., Nau, W.H., Gill, H., Bouley, D.M., Daniel, B., Rieke, V., Butts, R.K. & Sommer, G. 2004, "Highly directional transurethral ultrasound applicators with rotational control for MRI-guided prostatic thermal therapy", Physics in Medicine and Biology, vol. 49, no. 2, pp. 189-204.

Rouviere, O., Souchon, R., Salomir, R., Gelet, A., Chapelon, J.Y. & Lyonnet, D. 2007, "Trans-rectal high-intensity focused ultrasound ablation of prostate cancer: Effective treatment requiring accurate imaging", European Journal of Radiology, vol. 63, no. 3, pp. 317-327.

Rove K.O., M., Sullivan K.F., M. & Crawford D. E., M. 2010, "High Intensity Focused Ultrasound: Ready for Primetime", Urological Clinics of North America, vol. 37, no. 1, pp. 27-35.

Sapareto, S.A. & Dewey, W.C. 1984, "Thermal dose determination in cancer therapy", International journal of radiation oncology, biology, physics, vol. 10, no. 6, pp. 787-800.

Sapin-de Brosses, E., Gennisson, J., Pernot, M., Fink, M. & Tanter, M. 2010, "Temperature dependence of the shear modulus of soft tissues assessed by ultrasound", Physics in Medicine and Biology, vol. 55, no. 6, pp. 1701-1718.

Shariat, S.F., Raptidis, G., Masatoschi, M., Bergamaschi, F. & Slawin, K.M. 2005, "Pilot study of radiofrequency interstitial tumor ablation (RITA) for the treatment of radio-recurrent prostate cancer", The Prostate, vol. 65, no. 3, pp. 260-267.

Siegel, T., Moul, J.W., Spevak, M., Alvord, W.G. & Costabile, R.A. 2001, "The Development of Erectile Dysfunction in Men Treated for Prostate Cancer", The Journal of urology, vol. 165, no. 2, pp. 430-435.

Tan, J.S., Frizzell, L.A., Sanghvi, N., Wu, S., Seip, R. & Kouzmanoff, J.T. 2001, "Ultrasound phased arrays for prostate treatment", The Journal of the Acoustical Society of America, vol. 109, no. 6, pp. 3055-3064.

Tempany , C., Straus, S., Hata, N. & Haker, S. 2008, "MR-guided prostate interventions", Journal of Magnetic Resonance Imaging, vol. 27, no. 2, pp. 356-367.

Thoeny, H.C. & Ross, B.D. 2010, "Predicting and monitoring cancer treatment response with diffusion-weighted MRI", Journal of Magnetic Resonance Imaging, vol. 32, no. 1, pp. 2-16.

Tu, H., Jacobs, S.C., Borkowski, A. & Kyprianou, N. 1996, "Incidence of apoptosis and cell proliferation in prostate cancer: Relationship with TGF-β1 and bcl-2 expression", International Journal of Cancer, vol. 69, no. 5, pp. 357-363.

Uchida, T., Okusa, H., Yamashita, H., Shoji, S., Nagata, Y., Hyodo, T. & Satoh, T. 2006, "Five years experience of trans-rectal high-intensity focused ultrasound using the Sonablate device in the treatment of localized prostate cancer", vol. 13, no. 3, pp. 228-233.

Van Vulpen, M., Raaymakers, B.W., de Leeuw, A.A.C., Van de Kamer, J.B., Jeroen, A., Van Moorselaar, R., Hobbelink, M.G.G., Battermann, J.J. & Lagendijk, J.J.W. 2002, "Prostate Perfusion In Patients With Locally Advanced Prostate Carcinoma Treated With Different Hyperthermia Techniques", The Journal of urology, vol. 168, no. 4, pp. 1597-1602.

Von Ramm, O.T. & Smith, S.W. 1983, "Beam Steering with Linear Arrays", IEEE Transactions on Biomedical Engineering, vol. BME-30, no. 8, pp. 438-452.

Walsh, S.D.C., Saar, M.O., Bailey, P. & Lilja, D.J. 2009, "Accelerating geoscience and engineering system simulations on graphics hardware", Computers & Geosciences, vol. 35, no. 12, pp. 2353-2364.

Wiart, M., Curiel, L., Gelet, A., Lyonnet, D., Chapelon, J.Y. & Rouvière, O. 2007, "Influence of perfusion on high-intensity focused ultrasound prostate ablation: A first-pass MRI study", Magnetic Resonance in Medicine, vol. 58, no. 1, pp. 119-127.

Yin, X., Epstein, L.M. & Hynynen, K. 2006, "Noninvasive transesophageal cardiac thermal ablation using a 2-D focused, ultrasound phased array: a simulation study", Ultrasonics, Ferroelectrics and Frequency Control, IEEE Transactions on, vol. 53, no. 6, pp. 1138-1149.